HHS Public Access

Author manuscript

J Phys Chem B. Author manuscript; available in PMC 2020 December 31.

Published in final edited form as:

J Phys Chem B. 2020 July 09; 124(27): 5571–5587. doi:10.1021/acs.jpcb.0c03521.

Insulin dissociates by diverse mechanisms of coupled unfolding and unbinding

Adam Antoszewski[†], **Chi-Jui Feng**[†], **Bodhi P. Vani**[†], **Erik H. Thiede**[‡,P], **Lu Hong**[§], **Jonathan Weare**[‖], **Andrei Tokmakoff**[†,⊥,#], **Aaron R. Dinner**[†,⊥,#]

[†]Department of Chemistry, The University of Chicago, Chicago, Illinois

[‡]Department of Computer Science, The University of Chicago, Chicago, Illinois

[P]Department of Statistics, The University of Chicago, Chicago, Illinois

[§]Graduate Program in Biophysical Sciences, The University of Chicago, Chicago, Illinois

[‖]Courant Institute of Mathematical Sciences, New York University, New York, New York

[⊥]James Franck Institute, The University of Chicago, Chicago, Illinois

[#]Institute for Biophysical Dynamics, The University of Chicago, Chicago, Illinois

Abstract

The protein hormone insulin exists in various oligomeric forms, and a key step in binding its cellular receptor is dissociation of the dimer. This dissociation process and its corresponding association process have come to serve as paradigms of coupled (un)folding and (un)binding more generally. Despite its fundamental and practical importance, the mechanism of insulin dimer dissociation remains poorly understood. Here, we use molecular dynamics simulations, leveraging recent developments in umbrella sampling, to characterize the energetic and structural features of dissociation in unprecedented detail. We find that the dissociation is inherently multipathway with limiting behaviors corresponding to conformational selection and induced fit, the two prototypical mechanisms of coupled folding and binding. Along one limiting path, the dissociation leads to detachment of the C-terminal segment of the insulin B chain from the protein core, a feature believed to be essential for receptor binding. We simulate IR spectroscopy experiments to aid in interpreting current experiments and identify sites where isotopic labeling can be most effective for distinguishing the contributions of the limiting mechanisms.

Graphical Abstract

dinner@uchicago.edu.

Supporting Information Available

Supplementary figures (as referenced in the text) and accompanying commentary are available, as well as coordinate files for the structures shown in Figure 5 and used throughout this work.

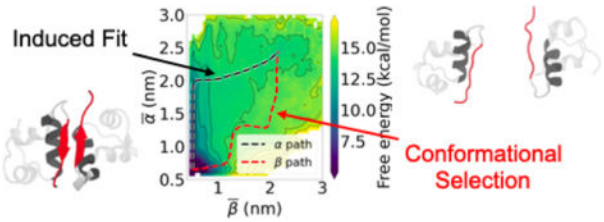

Introduction

Protein-protein association and dissociation are key to many cellular processes, ranging from transmembrane signaling[1–3] to endocytosis.[4] While some protein complexes may involve little (re)structuring of the participating components and thus conform to a lock-and-key model of molecular recognition, it is now clear that often (un)folding and (un)binding are coupled.[5–7] Coupled folding and binding can be described by two limiting mechanisms: induced fit, in which nonnative subunits form an initial encounter complex that then rearranges to a stable bound structure, and conformational selection, in which individual subunits first rearrange to conformations similar to those in the associated state and then bind.[8] Detailed characterizations of protein-protein association/dissociation simulations[9,10] suggest that coupled folding and binding is often multipathway, combining elements of both of these limiting mechanisms. This makes both experimental and computational study of coupled folding and binding challenging.

The protein hormone insulin has come to serve as a model for studying coupled folding and binding owing to its small size and the therapeutic importance of its equilibrium between different oligomeric states.[11–14] One such equilibrium is the one between dimer (Figure 1) and monomer. Each insulin monomer is 51 amino acids, organized into two polypeptide chains (A and B) joined by disulfide bonds (yellow in the left view). The 21-residue A chain forms two α helices (translucent), while the 30-residue B chain consists of an α helix (residues Ser^{B9}-Cys^{B19}, black) with a β turn (Gly^{B20}-Gly^{B23}, white) that leads to a C-terminal β sheet (Phe^{B24}-Ala^{B30}, red) in the dimer. Both experimental alanine scanning mutagenesis data[15] and free energy simulations[16,17] point to the importance of specific interfacial residues for stabilizing the dimer interface. These residues include the aromatic triplet of Phe^{B24}-Phe^{B25}-Tyr^{B26} on the interfacial β sheet,[13] Tyr^{B16} on the interfacial α helix, and both Gly^{B23} and Pro^{B28} on the β turn and the C-terminal segment of the B chain, respectively.

Dimer dissociation, which is a prerequisite for insulin to bind to its cellular receptor,[18] is thought to be an example of coupled unfolding and unbinding. While the dimer is well structured,[19,20] the monomeric state is thought to contain significant disorder. Specifically, experimental and computational studies indicate that Phe^{B24}-Ala^{B30} can detach from the B-chain α helix and become at least partially disordered in the monomeric state.[19,21–26] This detachment is thought to be important for insulin to bind its receptor[3,12,13] based on structures of insulin in complex with fragments of the receptor.[27,28] An outstanding question is how Phe^{B24}-Ala^{B30} detachment is coupled to dissociation of the dimer. More generally, the pathways of dimer dissociation remain poorly characterized. For example, it is unclear

what role, if any, the interfacial α helices play in dissociation, and whether there are partially solvated or unfolded intermediates.

There is some experimental evidence suggesting the dimer dissociation could couple unfolding to unbinding. In particular, temperature jump two-dimensional (2D) amide-I infrared (IR) spectroscopy measurements suggest that, during dissociation, there is conformational rearrangement within the monomers on the timescale of 5 to 150 μs, prior to loss of the β sheet at the dimer interface between 250 and 1000 μs.[24,25] Time-resolved X-ray scattering data also suggest an intermediate with conserved secondary structure on the timescale of 900 ns.[29] These experiments, although mechanistically suggestive, provide limited structural information; complementary simulations are needed to microscopically interpret these data.

Recently, Bagchi and coworkers used metadynamics to compute the free energy as a function of the monomer-monomer center-of-mass distance and the number of intermolecular contacts, subject to restraints on the radii of gyration of the monomers.[30–32] They identified a single major pathway of dissociation in which the number of intermolecular contacts was first observed to markedly decrease before the center-of mass distance increased. Through additional collective variables, they also characterized the protein-protein and protein-solvent interactions of Phe^{B24} and Tyr^{B26}, indicating that conformational rearrangement and intramonomeric unfolding are both coupled to the dissociation. Shaw and coworkers recently characterized the association of the insulin dimer through both unbiased simulation and tempered binding, an enhanced sampling technique that scales the protein interaction energies to encourage binding.[33] In contrast to the simulations described immediately above, they found that successful association events consisted of insulin monomers adopting conformations similar to those found in the dimer before binding, and observed very little intramonomeric unfolding. The extent to which these two binding/unbinding pathways, one which involves monomeric unfolding and one which does not, can coexist is currently unknown.

In this work, we use a computational pipeline that combines multiple methods for enhanced sampling of rare events in molecular dynamics simulations to investigate coupled unfolding and unbinding during insulin dimer dissociation. In particular, we identify collective variables that fully resolve the possible pathways for the dissociation, and we show how an error estimator that we recently introduced[34,35] can be used to quantitatively monitor convergence and allocate computational resources efficiently. The error estimator that we employ both provides quantitative evidence as to the convergence of our simulations, and allows us to meaningfully compare the free energy profiles of competing pathways by explicitly quantifying asymptotic errors. The computational pipeline enables us to show that there are multiple competing pathways for dimer dissociation, and we characterize these pathways in detail through additional collective variables that describe intra- and intermonomeric rearrangements. The pipeline is summarized in Figure 2 and at the start of the Results and Discussion section, so that readers interested primarily in the results can skip the Methods section without loss of continuity.

The limiting behaviors observed correspond to induced fit and conformational selection mechanisms. Our simulations thus provide a unified perspective on the binding/unbinding paths observed in previous simulations. We go on to propose a set of experiments to investigate the relative contributions of our limiting paths. Specifically, we simulate IR spectroscopy experiments for a variety of isotope-labeled insulins and identify two labels which, when measured via T-jump IR spectroscopy, could experimentally distinguish the contributions from the limiting pathways to dimer dissociation. These simulated IR spectra also provide references to which future measurements can be compared, facilitating the interpretation of both equilibrium and T-jump IR spectra for the insulin dimer.

Methods

With a view toward providing a quantitative interpretation of experimental observations, we model insulin in solution at atomic resolution (System Setup and Equilibration), such that dimer dissociation occurs on timescales that are long compared with the molecular dynamics timestep. Consequently, both efficient sampling and informative analysis rely on identifying collective variables (CVs) that capture the slowest relaxing degrees of freedom involved in dimer dissociation. To this end, we tested many combinations of CVs for their ability to enable us to harvest reactive events (String Method and Collective Variable Selection). We found that CVs based on selected intermolecular contacts in the dimer enabled us to harvest reactive events without the addition of restraints to prevent monomer unfolding, and we improved the contact definition over the course of the study, as we gained understanding of the system (Definition of Contacts). Care was taken to converge the potential of mean force (free energy) as a function of those CVs (Adiabatic-Bias Molecular Dynamics; Replica Exchange Umbrella Sampling; Eigenvector Method for Umbrella Sampling and Adaptive Sampling). We were able to trace multiple minimum free energy paths with comparable barriers on that surface, which we validated as stable through further simulations (Finding and Confirming Energetically Favorable Paths). Finally, we computed simulated infrared spectra to guide the design of further experiments (FTIR and 2DIR Simulation). These steps are summarized in Figure 2, and we describe each in detail below in the parenthetically indicated sections.

System Setup and Equilibration.

The system was modeled with the CHARMM36m force field.[36–38] All simulations were performed using GROMACS 5.1.4,[39] and the system was prepared using CHARMM-GUI 2.1.[40,41] Unless otherwise noted, simulations were carried out in the isochoric isothermal (NVT) ensemble at 303.15 K using a Langevin thermostat[42] with a 2 fs timestep and a friction constant of 0.5 ps^{-1} applied to all atoms. All bonds to hydrogen atoms were constrained using the LINCS algorithm[43]. Periodic boundary conditions were employed and the particle-mesh Ewald method[44] was used to calculate electrostatic forces with a cutoff distance of 1.2 nm. The Lennard-Jones interactions were smoothly switched off from 1.0 to 1.2 nm through the built-in GROMACS force-switch function. All molecular visualizations were done in VMD,[45] and residue interaction energies were calculated using its NAMDenergy plug-in.[46]

The dimer structure was based on the human insulin crystal structure (PDB ID 3W7Y).[47] To fully equilibrate the system at the desired temperature and pressure, the protein was solvated, equilibrated with restraints in both the NVT and isobaric isothermal (NPT) ensembles, and then equilibrated restraint-free in the NVT ensemble. Specifically, hydrogens were added to the PDB structure, and it was solvated in a cubic box of size (8 nm)^3 using TIP3P water[48]; 48 K^+ and 44 Cl^- ions were added to neutralize the system and bring it to a concentration of 150 mM KCl[49]. There was a total of 48,260 atoms. The system was energetically minimized using the steepest descent method, until the maximum force felt by the system was below 1000 kJ/mol nm. The system was then equilibrated for 100 ps in the NVT ensemble with a 1 fs timestep, followed by 10 ns in the NPT ensemble at 1 bar using the Parrinello-Rahman barostat,[50] with a 2 fs timestep and time constant of 5.0 ps. For the energy minimization and equilibration above, harmonic restraints were used to stabilize the positions of all non-hydrogen protein atoms. The system was equilibrated further for 1 ns in the NPT ensemble without position restraints, and the average box size was determined to be (7.82 nm)^3. This box size was used for all further simulations. The system was equilibrated once more without position restraints for 1 ns in the NVT ensemble. The resulting equilibrated structure, with a root-mean-square deviation (RMSD) of 2.02 Å from the 3WY7 crystal structure, was used to initialize further simulations as described below.

Definition of Contacts

Throughout the simulations in this work, relevant inter-residue α carbon distances were transformed by contact functions that smoothly vary between a small range of values. This was done to improve computational control in various methods, providing a consistent scale for biasing variables as distances varied between small and large values. The contact functions were tuned to each method, and as we learned more about the structural features of the dissociation. Specifically, we used the following three contact definitions to transform the distance between α carbons of residues i and j (d_{ij}):

$$s_{ij} = \left[1 - \left(\frac{d_{ij}}{\mathbb{E}[d_{ij}]}\right)^6\right] \Big/ \left[1 - \left(\frac{d_{ij}}{\mathbb{E}[d_{ij}]}\right)^{12}\right] \tag{1}$$

$$s_{ij} = \begin{cases} 1 & \text{if } d_{ij} < \mathbb{E}[d_{ij}] \\ \exp\left(\frac{-(d_{ij} - \mathbb{E}[d_{ij}])^2}{2r_0^2}\right) & \text{otherwise} \end{cases} \tag{2}$$

$$s_{ij} = \begin{cases} 1 & \text{if } d_{ij} < \mathbb{E}[d_{ij}] \\ 1 - \tanh\left(\frac{d_{ij} - \mathbb{E}[d_{ij}]}{\gamma d_{\text{mon}}}\right) & \text{otherwise} \end{cases} \tag{3}$$

In the above equations, $\mathbb{E}$ denotes an equilibrium average, and the average distance $\mathbb{E}[d_{ij}]$ was measured for each contact pair from a 5 ns simulation, initialized from the equilibrated dimer structure. The definition in Equation 1 was used for the initial driving and string

method simulations used to discover collective variables. The definition in Equation 2 was used for the umbrella sampling calculations, as it provided a gentler bias near the dimer state. In this definition, r_0 is a parameter that sets the location of the inflection point of the Gaussian transformation. This parameter was set to 0.6 nm to ensure that there were at least three layers of water between all monomeric residues at dissociation, based on visual inspection. Finally, the definition in Equation 3 was used for the final string calculations used to verify the stability of our observed low-energy paths, as it provided better resolution near the dimer state. In this definition, d_{mon} is the average residue pair distance that corresponds to the monomeric state, again chosen so that at least three layers of water separate the residues of interest. This was thus set to be 2.2 nm for the α contacts and 2.0 nm for the β contacts (see Results). The parameter choice $\gamma = 0.65$ tunes the sizes of the monomeric and dimeric states in the 2D contact space.

String Method and Collective Variable Selection.

Umbrella sampling is predicated on finding a small number of collective variables (CVs) that capture the slowest relaxing degrees of freedom relevant to the process of interest. To determine reasonable CVs for insulin dimer dissociation, we tested various combinations of CVs for their ability to drive dissociation in steered molecular dynamics simulations (SMD)[51] and then selected CVs that preserved the ability to distinguish refined dissociation paths obtained from the string method,[52,53] discussed in further detail below. The CVs explored were based on interacting pairs of residues with high differential solvent accessible surface area (SASA) between dimer and monomer states (Supplemental Table S1, where the apostrophe differentiates residues on one monomer from residues on the other). These included the aromatic triplet in the interfacial β sheet, which was previously identified as important for dimer stability.[17,19,54]

Distances between the C_α atoms of these residue pairs were computed and transformed using Equation 1 as described above. Constant velocity SMD simulations, in which harmonic restraints were used to advance random subsets of s_{ij} from 0.5 to 0.0, were used to drive the system from the equilibrated dimer structure to the dissociated state. By visual analysis, we selected dissociation paths that both led to complete dissociation and did not involve significant unfolding of the monomers since there is limited experimental evidence for extensive loss of secondary structure.[25,29] We also only selected paths that had maximum free energies within the range of previous simulations.[19,30] These were used to initialize string method simulations in the 22-dimensional space of intermonomeric contacts described above (Supplemental Table S1). Convergence of strings during the simulations was computed by the Hausdorff distance metric between the current string iteration and the initial string, and simulations were run until this distance metric did not change significantly.[55]

To choose a small number of CVs sufficient to describe the dissociation, we clustered the initial and final strings in the space of the first few coordinates obtained from applying the diffusion maps method[56,57] to their images. We then sought physically interpretable CVs that preserved the clusters, which led to selection of two average contact functions (averaging performed after the transformation), one for three residue pairs at the β sheet

interface ($\overline{\beta_c}$) and one for seven residues at the α helical interface ($\overline{\alpha_c}$). These are detailed in Supplemental Table S1 and Figure 3. These residue pairs are consistent with important interfacial interactions identified in a recent steered molecular dynamics study.[17] We denote the average of the raw distances associated with $\overline{\beta_c}$ and $\overline{\alpha_c}$, used for visualization, by $\bar{\beta}$ and $\bar{\alpha}$, respectively.

Adiabatic-Bias Molecular Dynamics (ABMD).

To initialize sampling, 49 independent ABMD[58] molecular dynamics simulations (using the PLUMED 2.3 wrapper for GROMACS[59–61]) were used to drive the system from the dimer to a 7 × 7 grid of points evenly covering the 2D CV space of $\overline{\beta_c}$ and $\overline{\alpha_c}$. ABMD is similar to SMD but ratchets the system to its target following unbiased fluctuations along the CVs; we came to prefer it to SMD because we found that SMD but not ABMD resulted in melting of the interfacial α helices. That said, because ABMD relies on unbiased fluctuations, we found that the initial simulations did not adequately sample the space close to the $\overline{\beta_c} = 0$ and $\overline{\alpha_c} = 0$ axes. We thus performed 13 extra simulations to drive the system to supplementary points near where either one or both of $\overline{\beta_c}$ or $\overline{\alpha_c}$ went to zero. This driving, whose bias was applied on the 10 individual distances associated with $\overline{\beta_c}$ and $\overline{\alpha_c}$, was repeated with force constants of 1000, 3000, and 5000 kJ/(mol nm), generating a database of trajectories that covered all of the relevant average contact space.

Replica Exchange Umbrella Sampling (REUS).

The window centers for the umbrella sampling were distributed on a logarithmically spaced grid in the space of $(\overline{\beta_c}, \overline{\alpha_c})$ with the expectation that the initial steps of the dissociation would involve larger changes in free energy, as seen in Figure 4A. The force constants, k, for the harmonic biases associated with each window were described by the following equation, adapted from an expression derived by Im and coworkers:[62,63]

$$\sqrt{k} d_{\max} = 0.8643 \sqrt{2 k_B T} . \quad (4)$$

Here, as the windows are unevenly spaced, $d_{\max}$ refers to the maximum distance between adjacent window centers. Additional weak upper walls (half harmonic potentials with $k = 50$ kJ/(mol nm), turned on at 3 nm for each distance) were placed on each distance to prevent artificial interactions across periodic boundaries. To initialize each window, the ABMD-generated structure that was nearest to each minimum was selected and equilibrated for 100 ps using the harmonic restraint described by equation 4. A 2D replica exchange procedure, in which there were exchanges between windows,[64] was implemented by taking advantage of the built-in functionality of GROMACS. Each of the 784 windows were simulated for 100 ps, with exchanges attempted at 1 ps intervals only between adjacent windows in the same row. The windows were then simulated for an additional 100 ps, with exchanges attempted every 1 ps between adjacent windows in the same column. This procedure was repeated for a total of 5 ns of simulation time per window, with structures saved every 5 ps. In this way, replicas were exchanged via all nearest neighbors across the entire lattice of windows. Exchange probabilities between 10–50% were achieved depending on the specific window pairs being swapped.

Eigenvector Method for Umbrella Sampling (EMUS) and Adaptive Sampling.

The 5 ns of sampling per window was combined to generate a potential of mean force (PMF) by using the Eigenvector Method for Umbrella Sampling (EMUS).[34] Once the PMF was created, we wanted to investigate whether the PMF was converged and, if not, add additional sampling selectively where it would be most effective. To do this, EMUS was used to estimate the asymptotic variance of replica exchange umbrella sampling simulations. However, because of the replica exchange, assumption VII.3 of ref. 34, namely that sampling in each window is independent, does not hold for our study. Nonetheless, one can still apply Lemma VII.2 in ref. 34 to derive a central limit theorem for EMUS with replica exchange by casting sampling over all windows as a Markov chain; in this case, the asymptotic covariance matrix, Σ, is not block diagonal. This leads to a definition of the asymptotic variance for arbitrary averages that one can approximate by an expectation of integrated autocovariances over the sampled data. For details, see the Supplemental Information.

The contact space PMF is shown in Figure 4B, with its associated asymptotic variance in Figure 4C. The area of highest asymptotic variance in the PMF was identified, and is marked by a red box in Figure 4C. Using the process described in ref. 34, the per-window error contributions to this region were determined; although these include only the error we would observe if the off-diagonal blocks of Σ were zero, we believe they are sufficient to diagnose the behavior of the umbrella sampling scheme. These contributions are shown in Figure 4D, and reveal a J-shaped region of windows which contribute the most to the asymptotic variance of the region marked in Figure 4C. These windows were then identified as areas to add additional sampling. This additional sampling used a similar procedure as described above for the initial replica exchange simulations, with the sampling and proposed exchanges restricted to the bottom-most five rows and right-most 5 columns in Figure 4D. At 1 ns intervals, this additional sampling was independently processed with EMUS as follows. These data were used to compute a new PMF and its associated asymptotic variance per bin, $\sigma^2_{ij,\,\mathrm{supp}}$. We then combined $\sigma^2_{ij,\,\mathrm{supp}}$ with the initial asymptotic variance, $\sigma^2_{ij,\,\mathrm{ini}}$, weighted by the squared ratio of simulation lengths between supplemental and total sampling, f^2_{supp}:

$$\sigma^2_{\mathrm{tot}} = f^2_{\mathrm{supp}}\sigma^2_{ij,\,\mathrm{supp}} + \left(1 - f_{\mathrm{supp}}\right)^2\sigma^2_{ij,\,\mathrm{init}} \tag{5}$$

Equation 5 assumes the initial 5 ns and supplemental 5 ns of sampling are independent, which given that the autocorrelation time of the quantities needed for EMUS was 6 ps on average across the windows, is a reasonable assumption.

As seen in Figure 4E, the peak variance decreased from 0.25 to 0.12 $(\mathrm{kcal/mol})^2$ upon the addition of 5 ns of additional sampling per window in the outlined J-shaped region. This region would not obviously be chosen in the absence of a quantitative procedure, though it can be rationalized in hindsight as corresponding to a major dissociation pathway that we characterize in detail in Results and Discussion. This illustrates how EMUS allows users to monitor the convergence of US simulations as sampling proceeds, and to adaptively identify regions of state space that are most in need of additional sampling, despite the neglect of

correlations discussed above. Furthermore, EMUS allows for the calculation of PMFs in arbitrary CV spaces, not just the space in which the biasing was done, without the need for additional sampling. Examples of these PMFs are seen in Results and Discussion.

Finding and Confirming Energetically Favorable Paths.

Our analysis of dissociation is based on minimum free energy paths. Initially, seven such paths were drawn on the 2D PMF by using the lfep search algorithm.[65] To ensure that these were stable in the 10-dimensional space of all of the contacts associated with the averages $\overline{\alpha_c}$ and $\overline{\beta_c}$, another iteration of the string method was run in this space, this time initialized from structures drawn from the REUS database along these 2D minimum free energy paths. The specific contact definition used is in Equation 3, and the strings were run until converged as measured by the Hausdorff distance, as discussed previously. The starting and ending positions of these strings are shown in Supplemental Figure S1. In particular, the α path shows almost no variation, and the β path shifts only minimally, and this shift does not change any of the molecular trends discussed in the Results. The others paths also exhibit minimal variation. This provides evidence that most of the pathways we identify and the limiting pathways in particular are indeed stable in a broader space.

FTIR and 2DIR Simulation.

Simulated IR spectra were calculated from the Fourier transform of a vibrational transition dipole time correlation function using a mixed quantum-classical model described in refs. 66 and 67. Briefly, electrostatic collective variables can be used to translate molecular-dynamics sampling of protein structure into (i) a time-dependent Hamiltonian and (ii) a transition dipole moment that describes the amide I vibrations of protein backbones; these quantities in turn can be used to calculate the dipole time correlation functions that are needed to create simulated FTIR and 2D IR spectra. Furthermore, these spectra can be calculated for both native proteins and isotope-labeled proteins.[68] Here, we aimed to generate FTIR spectra for 50 points equally spaced along both the α and the β paths for a variety of isotope-labeled insulins. 2DIR spectra were then calculated for specific states for two isotope-labeled insulins. These spectra were then used to propose possible experiments to validate our results.

First, each path was divided into a series of 50 points, referred to as image centers. By comparing these image centers to the REUS database, 20 structures were selected to be associated with each image center. These structures were randomly drawn from the sampling that was within both 0.4 nm of each image center and the Voronoi tessellation associated with each image center. Each of these structures served as the starting point for an additional short molecular dynamics simulation consisting of 100 ps of equilibration followed by 100 ps of sampling every 20 fs. These simulations were then used to generate both the FTIR and 2DIR spectra by using the procedure outlined below.

As IR spectra correspond to manifestly quantum-mechanical vibrational transitions, our classical molecular dynamics trajectories had to be translated into a time-dependent Hamiltonian and transition dipole trajectories. To this end, we associated each amide I vibration with a site, defined by the atomic positions of the backbone amide groups (C, O,

N, and H atoms). The frequency of each site was calculated using an empirical electrostatic frequency map optimized against experimental spectra of isotope-edited NuG2b protein, which evaluates the electrostatic potential value at the C, O, N, and H positions.[69] This potential-based map (4PN-150) has an estimated frequency uncertainty of 2.25 cm^{-1}. When applying the map, we used modified glycine charges described previously.[69] Additionally, we considered coupling between sites, including both through-bond mechanical coupling and through-space electrostatic coupling. Through-bond coupling between adjacent sites was generated using a density functional theory (DFT)-based nearest-neighbor coupling map, while through-space coupling was computed by a transition charge coupling map.[70] We did not account for vibrations from protein side-chain and terminal groups. The transition dipole of each site was assigned using the zero-field values from a DFT-based electrostatic map.[71] When generating simulated 2DIR spectra, there are signal contributions from excited state absorption (ESA), which correspond to vibrational transitions between states with one quantum of excitation energy and those with two quanta of excitation energy. To deal with this, the corresponding two-quantum Hamiltonian and transition dipole moments were constructed using a weak anharmonic model.[66,72]

The time-dependent Hamiltonian and transition dipole trajectories were converted to simulated FTIR spectra and 2D IR spectra using a dynamic wavefunction-propagation scheme with a Trotter expansion to reduce computation time.[73,74] The window time for calculating dipole time correlation functions was set to 2.5 ps. The anharmonicity of the amide I oscillator was set to 16 cm^{-1}.[72] The amide I vibrational lifetime was modeled by an ad hoc single exponential decay, with a time constant of 1.0 ps determined by transient absorption experiments of Ala–Ala.[75] The isotope frequency shift introduced by a $^{13}C^{18}O$ label was set to 65 cm^{-1}.[66] The spectra for the structures that were selected from the REUS database were uniformly averaged within each of the 50 images across both paths. This created a simulated spectrum representative of the location of each image in CV space. The isotope labeled FTIR spectra along each path, with the corresponding simulated unlabeled spectra subtracted to create difference spectra, are shown in Supplemental Figure S2. Based on these results, the data were regrouped and reaveraged as described in the Supplemental Information to create the 2DIR spectra shown in a future section.

Results and Discussion

Our goal was to investigate the molecular changes in intra- and intermolecular structure during insulin dimer dissociation. To this end, as summarized in Figure 2 and detailed in Methods, we first used steered molecular dynamics to generate multiple dissociation events, naively biasing the simulations to force the monomers apart. We then refined the resulting paths with the string method, which relaxes these paths to local minimum free energy paths. Based on these simulations, we identified a small number of distances that provided good control over sampling (specifically, replica exchange umbrella sampling): 7 between C_α atoms in the interfacial α helices and 3 between C_α atoms in the interfacial β sheet (Figure 3). The α and β distances were separately averaged to define collective variables $\bar{\alpha}$ and $\bar{\beta}$, respectively. We used replica exchange umbrella sampling together with an error estimator that we recently introduced[34] to ensure good sampling of configurations consistent with each combination of these variables. From these data, we constructed the PMF as a function

of the average interfacial distances. Below, we describe this PMF, followed by additional statistical averages that provide further insights into specific intra- and intermolecular structural features. We conclude by showing how simulated vibrational spectra can serve as references for the design and interpretation of experiments.

Dissociation is multipathway, with two limiting cases.

The PMF as a function of $\bar{\alpha}$ and $\bar{\beta}$ is shown in Figure 5, surrounded by representative structures. The minimum of the dimeric basin is marked by the circle at $(\bar{\beta}, \bar{\alpha}) = (0.53, 0.63)$ nm, and we set it to be the zero of free energy. The dimer is flanked by a trough along each axis, corresponding to breaking the β contacts while maintaining the α contacts and vice versa. There is a shoulder at $\bar{\beta} \approx 0.75$ nm; calculations described further below show that it coincides with solvent penetration of the β sheet. The remainder of the PMF is relatively flat. We take the monomeric state to be $\bar{\beta} > 2.0$ nm and $\bar{\alpha} > 2.2$ nm. (marked by the dotted white box in Figure 5), which ensures that there are at least three layers of water between interfacial residues (see Methods). The free energy in this region ranges from 13 to 15.5 kcal/mol, within the range of previous estimates of the stability of the dimer.[16,17,30,76] The plateau surrounding the monomeric state is between 1–3 $k_B T$ higher in free energy.

Consistent with the diversity of paths that we obtained in our steered molecular dynamics and string method simulations (see Methods), many minimum free energy paths can be drawn on the PMF (Supplemental Figure S1). These paths are stable not only in this 2D average distance space, but also the full 10-dimensional space of all individual distances, as indicated by the string method results in Supplemental Figure S1. Despite their similar maximum free energies, these paths imply dramatically different mechanisms of dissociation. For clarity, we focus on two limiting cases that initially follow the aforementioned troughs in free energy flanking the dimer. Along the α path (black in Figure 5), the interfacial α helices separate prior to the strands of the β sheet; along the β path (red in Figure 5), the order is reversed.

The free energy profile of the α path is consistent with the minimum free energy path obtained by Bagchi and coworkers (compare the black lines in Supplemental Figure S3 with Paths 1 and 4 in Figure 3 of ref. 30): there is an initial rise to an intermediate of 7.7 kcal/mol (5.3 kcal/mol in ref. 30), followed by a shoulder ~2.4 kcal/mol higher in free energy and then a barrier of ~4.0 kcal/mol. The free energy profile of the β path exhibits no comparable shoulders, but its maximum is comparable to that of the α path (14.7 kcal/mol and 14.1 kcal/mol, respectively). Considering the typical asymptotic variance of our PMF is on the order of 0.2 $\text{kcal}^2/\text{mol}^2$, we thus expect both of these limiting paths, as well as the many paths that fall between them (Supplemental Figure S1), to contribute to dissociation.

The monomers rotate relative to each other in opposite ways along the two limiting paths.

Previous studies[30,31] reported rotation of the interfacial β strands relative to each other, as characterized by a pseudodihedral angle (here denoted Φ_β) defined by the C_α atoms of Tyr^{B26}, Phe^{B24}, $\text{Tyr}^{B'26}$, and $\text{Phe}^{B'24}$, where the primes distinguish one monomer from the other. In addition to Φ_β, we calculate the pseudodihedral angle (Φ_α) between the geometric

centers of the backbone atoms of the residues that define the dimeric interfacial alpha helices: Ser^{B9}- Leu^{B11}, Leu^{B17}-Cys^{B19}, Leu$^{B'17}$-Cys$^{B'19}$, and Ser$^{B'9}$-Leu$^{B'11}$. Explicit illustrations of these angles are shown in Supplemental Figure S4. By examining both Φ_β and Φ_α, we can better understand whether the rotation is restricted to the β strands, or if the entire dimer interface moves together. Since molecular dynamics simulations allow any collective variable to be calculated within machine precision, we create PMFs in four 2D spaces that measure interfacial rotations as both $\bar{\alpha}$ and $\bar{\beta}$ change (Figure 6A); the plots are restricted to ranges of $\bar{\alpha}$ and $\bar{\beta}$ that correspond to the initial steps of dissociation because the interfacial pseudodihedrals become poorly defined when the average distances are large. All of the PMFs, both in Figure 5 and Figure 6, are generated from the same dataset, as EMUS allows for the calculation of PMFs in arbitrary collective variable spaces without the need for additional sampling.

There is a deep free energy basin corresponding to the dimer at $(\bar{\beta}, \bar{\alpha}) = (0.58, 0.63)$ nm and $(\Phi_\beta, \Phi_\alpha) = (-15°, 125°)$. This reflects the fact that in the dimer state, in agreement with available crystal structures, there is a slight rotation from parallel between the β sheet residues, and a more pronounced rotation between α helices, consistent with well-known characterizations of α helix packing.[77–79] The PMFs are dominated by the troughs flanking the dimer in Figure 5. The trough along the α path (black dotted arrows) is readily visible in both sets of plots and shows that increases in $\bar{\alpha}$ are coupled to negative rotations of both Φ_α and Φ_β (by −35° and −45°, respectively). The trough along the β path (red dotted arrows) is more readily visible in the bottom plots and shows that increases in $\bar{\beta}$ are coupled to positive rotations of Φ_β; there is little change in Φ_α, suggesting the interfacial α helical contacts are maintained. Side views (similar to the middle panel of Figure 1) of the dimer and rotated species show the structural consequences of these interfacial rotations (Figure 6B). Namely, comparing these side views with the corresponding front views (Figure 5) suggests that the initial dissociation along the limiting β path involves the breaking of the interfacial β sheet and the positive rotation of Φ_β. In contrast, the initial dissociation along the α path comes as the α helices twist away from each other, coupled with negative rotations of both Φ_α and Φ_β.

The negative rotations along the α path enable formation of nonnative interactions (Figure 6C). The serine side chains of Ser^{B9} and Ser$^{B'9}$ (yellow in Figure 6C) form a hydrogen bond at $\bar{\alpha} \in [1.0, 1.3]$ nm. Then, as the β strands rotate relative to each other along the α path, Pro^{B28}-Ala^{B30} (pink) breaks its native contacts and instead forms a contact with tyrosine Tyr$^{B'16}$ (gray), in the α helix of the opposite monomer. This tyrosine at Tyr^{B16} contacts Ser^{B9}, Val^{B12}, and Tyr$^{B'26}$ in the dimeric state (see Supplemental Table S1), but these interactions are broken as the α helices separate. Averages of side chain contacts that quantitatively show these trends are seen in Supplemental Figure S5. Furthermore, the necessity of breaking the native contacts between Pro^{B28}-Ala^{B30} and Gly$^{B'20}$-Gly$^{B'23}$ as the dissociation progresses is consistent with the mutations that yield fast-acting insulin analogs, discussed further in the Supplemental Information (Supplemental Figure S6). No comparable nonnative interactions are observed along the β path.

These projections further allow us to compare with Bagchi and coworkers' results. In particular, Figure 8 of ref. 31 indicates a path which begins with a slight increase in Φ_β

coupled to an increase in $\bar{\beta}$ from approximately 0.6 to 1.1 nm. This initial step is followed by a 30° decrease in Φ_β coupled to a return to a dimer-like $\bar{\beta}$ (near 0.6 nm) as the dissociation progresses. The β strands only separate at the final step of their described mechanism. We interpret this to correspond to taking an initial step along the β path, then collapsing back to a near-dimer like β interface before proceeding along the α path. That said, the projections of the α and β paths onto Bagchi and coworkers' coordinates do not fall precisely on top of their minimum free energy path (Supplemental Figure S7). By explicitly probing the multipathway nature of the dissociation, our results reveal the homogeneity of rotation profiles depending on dissociation path.

Water solvates key interfacial residues as dissociation progresses.

Solvent plays a key role in protein association/dissociation processes. Moreover, time resolved X-ray scattering data suggest at least one intermediate in the insulin dimer dissociation that involves quick solvent uptake by a species with dimer-like secondary structure, coincident with a slight increase in molecular volume.[29] To investigate the possible presence of a similar feature in our simulations, we defined three collective variables; in order of increasing specificity, they are (i) the total molecular volume, (ii) the solvent accessible surface area (SASA) of eight residues that make up the hydrophobic core of the interface (Val^{B12}, Tyr^{B16}, Phe^{B24}, Tyr^{B26} on each monomer), and (iii) the number of native interfacial hydrogen bonds, which only form between Phe^{B24} and Tyr^{B26}. The total molecular volume, probed by the X-ray scattering, can reflect solvent uptake, but it can also correspond to large-scale conformational change. The core SASA reflects the solvation of the interface in general, while the hydrogen bonding between interfacial residues probes the loss of dimer-like secondary structure. Averages of these variables are seen in Figure 7A.

The red and red black dots in Figure 7A mark the positions of the structures in Figure 7B, which show characteristic solvations of the β and α interfaces, respectively. These structures represent low free energy states relative to the barriers along the β or α paths. Moving from the dimeric state to either of these positions, the total molecular volume increases by 0.3–0.4 nm^3. This small increase in molecular volume allows some solvation of the interface, increasing core SASA by between 0.8–1.2 nm^2. Along the α path, this solvation is at the α interface, while, along the β path, this solvation is at the β interface (Figure 7B). The former does not result in a loss of secondary structure as measured by STRIDE.[80] By contrast, we do see a distinct loss of β sheet content along the β path. Specifically, as $\bar{\beta}$ increases, the Phe^{B24} and Tyr^{B26} hydrogen bonds across the interface are replaced with ones to solvent (white contour in the right panel in Figure 7A and Supplemental Figure S8), signaling the loss of the interfacial β sheet.

One would expect that the loss of the interfacial β sheet and the solvation of the hydrophobic core are highly correlated because the separation of the β strands would allow water to penetrate between the monomeric units. We observe this to be the case when the α helices are already partly separated ($\bar{\alpha} > 1.0$ nm). The breaking of the interfacial hydrogen bonds, represented by the white contour in the right panel of Figure 7A, occurs in the same area of the collective variable space as the rapid solvation of the hydrophobic core, represented by the tight black contours in the middle panel of Figure 7A. This area, where $\bar{\beta} \approx 0.75$ nm, is

also co-located with the shoulder in the PMF mentioned earlier (Figure 5), suggesting that the loss of β sheet content and concomitant solvation gives rise to a slight decrease in free energy. The stabilization that we observe is consistent with previous simulations of mutants of the insulin dimer which indicate that water can mediate β sheet interactions by forming hydrogen bonds that bridge between residues.[76] The existence of this shoulder is also consistent with states involved in the dewetting transition seen in ref. 32, in which the center-of-mass separation of the monomers is 2 nm and there are a few water molecules at the interface.

However, when the α helices are in a near-native distance ($\bar{\alpha} < 1.0$ nm), the solvation of the hydrophobic core occurs after the loss of the interfacial β sheet. In this case, the protein-protein hydrogen bonds are broken when $\bar{\beta} \approx 0.65$ nm (white contour in the right panel of Figure 7A) but the hydrophobic core residues do not become significantly solvated until the β strands are even further separated, at approximately $\bar{\beta} = 0.9$ nm (middle panel of Figure 7A). This occurs within a low-free-energy trough of the PMF; in other words, the PMF only rises sharply as the core is solvated, not with the loss of hydrogen bonds. Evidence of these dynamics are further seen in the simulated IR results presented later, in which the peak absorption/emission doublet is red shifted with only a minimal loss in intensity.

As mentioned in the introduction, Chen and coworkers found evidence for a partially-solvated intermediate with dimer-like secondary structure, implying conserved interfacial β sheet character.[29] Although we find no distinct free energy basin that obviously corresponds to this intermediate, the initial partially solvated structures we observe along the α path are consistent with these data, as the interfacial β sheet is conserved. However, even with the loss of the β sheet along the β path, our simulations do not rule out the possibility of structures along the β path also being consistent with the X-ray scattering data. Specifically, the experimental data were collected at 316 K and 0.27 M DCl (pH ≈ 0) in a solution of ethanol and water, while our simulations are for 303.15 K and pH 7 with only water as the solvent. Previous computational work suggests that ethanol appears to facilitate partial solvation of the β interface,[31] so further simulations are needed to definitively interpret these T-jump X-ray scattering experiments.

The B-chain C-terminal segment detaches along the α path but not the β path.

As noted above, there is extensive evidence that the B-chain C-terminal segment must detach from the B-chain α helix for insulin to bind its receptor.[13,27,28,81,82] Detachment and partial unfolding have also been invoked to explain the diagonal elongation of features in equilibrium 2D infrared spectra of insulin at elevated temperatures.[24] Whether detachment and partial unfolding occurs during dissociation remains an open question.

These considerations, combined with the known partial disorder of the β turn and the B-chain C-terminal segment in the insulin monomer,[22–24,26] motivated our definition of two average angles to study intramonomeric unfolding during dimer dissociation: $\overline{\Psi_d}$, which measures detachment of the B-chain C-terminal segment from the B-chain α helix, and $\overline{\Psi_t}$, which characterizes the disorder of the β turn. Results for $\overline{\Psi_t}$ are discussed in the Supplemental Information (Supplemental Figure S9); here we focus on $\overline{\Psi_d}$. $\overline{\Psi_d}$ is the angle

between the C_α atoms of Arg^{B22}, Phe^{B24}, and Tyr^{B26} (Supplemental Figure S10), measured for each monomeric unit and then averaged. $\overline{\Psi_d} = 180°$ indicates an attached structure, because a flat β strand tucks against the B-chain α helix. In contrast, $\overline{\Psi_d} = 90°$ indicates a structure that is almost completely detached, with the B-chain C-terminal segment bent away from the α helix. This detachment is also coupled to the solvation of Gly^{A1}-Val^{A3}, which are involved in binding to the insulin receptor[20] (Supplemental Figure S11). Examples of monomeric structures with attached and detached B-chain C-terminal segments are shown in Figure 8A. Figure 8B shows the full dimer view of the same detached intermediate with $\Psi_d = 140°$ to illustrate how the detachment of the C-terminal segment allows for the nonnative interaction of Pro^{B28}-Ala^{B30} and $Tyr^{B'16}$, the same nonnative interaction shown in Figure 6C.

The average value of Ψ_d as a function of $\bar{\alpha}$ and $\bar{\beta}$ is plotted in the left panel of Figure 8C. The dimer state corresponds to $\overline{\Psi_d} = 172°$, consistent with the β strand being attached. $\overline{\Psi_d}$ decreases significantly along the α path; the latter half of the path ($\bar{\alpha} > 1.5$ nm) consists mainly of structures in which the B-chain C-terminal segment is detached ($\overline{\Psi_d} < 165°$). This behavior contrasts with the β path, in which the minimum value of $\overline{\Psi_d}$ is $\overline{\Psi_d} = 167°$ (we neglect the low values of $\overline{\Psi_d}$ in the lower right corner of Figure 8C because that region is very high in free energy; see Figure 5). Overall, while we observe some detachment along the β path, it is much more pronounced along the α path. It is also worth noting that in the monomeric region identified earlier ($\bar{\beta} > 2.0$ nm and $\bar{\alpha} > 2.2$ nm) the detachment is less pronounced than at intermediate stages of the α path. However, the monomeric region has more variability in detachment angle than in the dimeric region, consistent with previous results showing a limited amount of disorder in the C-terminal segment of the B chain.[22–24,26]

Along the β path, instead of unfolding, the β sheets separate and the monomers drift away from one another, forming a diverse set of non-specific, nonnative interfacial contacts, as in structure 2β in Figure 5. The numbers of native and nonnative interfacial contacts are plotted in the center and right panels of Figure 8C, respectively. Along the β path (red), the native contacts are almost completely broken as $\bar{\beta} > 1.0$ nm, although a limited number of nonnative contacts persist as the dissociation proceeds further. Similarly, along the α path (black), we also see the formation of nonnative contacts coupled to the breaking of native contacts, consistent with the side-chain interactions discussed previously (Figure 8B).

Finally, we note that T-jump 2D amide-I IR spectroscopy experiments in 20% ethanol indicated two contributions to the dimer dissociation process: melting of the dimer β sheet observed between 250–1000 μs, and a 5–150 μs process that was assigned to α helix disordering.[25] These timescales thus suggest that unfolding occurs before the loss of the interfacial β sheet. In our (aqueous) simulations, we do not observe any loss of α helix content, although it may be possible that helix rotation could give rise to such a signal. Instead, the unfolding that we observe is restricted to detachment of the B-chain C-terminal β strand and disorder of the β turn (see Supplemental Figure S9), which primarily occurs along the α path. Furthermore, the detachment along the α path (following the black path in the left panel of Figure 8C) starts to occur before the loss of the interfacial β sheet (right

panel of Figure 7A). The α path, which exhibits monomeric unfolding in the form of C-terminal detachment while maintaining dimer-like secondary structure, is thus consistent with the T-jump data gathered by Tokmakoff and coworkers.[25] Moreover, this detached state also corresponds to an increase in molecular volume of between 0.6 and 0.8 nm^3, which is consistent with the evidence from Chen and coworkers for a second intermediate that corresponds to a large increase in molecular volume while maintaining secondary structure.[29]

The α and β path correspond to induced fit and conformational selection.

In this section, we connect the intramonomeric detachment and core solvation with the intermonomeric rotations discussed earlier to characterize the various mechanisms of the insulin dimer dissociation, making explicit comparisons to the induced fit and conformational selection models of coupled folding and binding. A summary is shown in Figure 9.

The α path, as mentioned before, initially consists of rotations at both the α and β interfaces (Figure 6A); the alpha helices twist away from each other, forming nonnative contacts between Ser^{B9}:$Ser^{B'9}$ and Pro^{B28}-Ala^{B30}:$Tyr^{B'16}$ (Figure 6C). This initial α helix separation and rotation increases the SASA of the hydrophobic core by ~1.5 nm^2, while further α helix separation (between $\bar{\alpha} = 1.0$ nm and $\bar{\alpha} = 1.35$nm) leads to very little additional core solvation (Figure 7A). This solvation correlates with the free energy along the α path, which also sharply increases until $\bar{\alpha} = 1.0$ nm, where it levels off around 8 kcal/mol until $\bar{\alpha} = 1.35$nm (Figure 5). There is then another free energy barrier of 2 kcal/mol when $\bar{\alpha} \in [1.35, 2.0]$ nm, which correlates well with the β sheet starting to detach from the core (Figure 8C). This detachment, while partially maintaining the nonnative interactions between Pro^{B28}-Ala^{B30}:$Tyr^{B'16}$, sacrifices native contacts and exposes Gly^{A1}-Val^{A3} to the solvent (Supplemental Figure S11). The last barrier of 4 kcal/mol correlates to the breaking of the interfacial β sheet hydrogen bonds and the subsequent separation of the β strands. Structurally this final step is heterogeneous, involving varying amounts of detachment, rotation, and sliding of the β strands as $\bar{\beta}$ increases.

In terms of the association process, the α path corresponds to the induced fit model of coupled folding and binding. Following the black trace in Figure 8C from monomer to dimer (top right to bottom left), association is initiated by the B-chain C-terminal strands detaching and encountering one another. The β interface becomes structured; then, the α helices are recruited into the interface, leading to a dimer-like structure. The monomers only adopt their structures in the dimer upon association.

The β path first couples the initial separation of the β strands to their rotation (Figure 6A). This correlates to the sudden increase in free energy from 0 to 14 kcal/mol as $\bar{\beta}$ increases from 0.5 to 1.2 nm. The subsequent steps of the dissociation correspond to the two monomers, with conformations similar to the ones found in the dimer, drifting away from one another. Specifically, as the dissociation proceeds, a diverse set of nonnative interfaces are formed that are structurally close to the native interface, but involve minimal detachment of the B-chain C-terminal segment (Figure 8C). This is consistent with the relatively flat free

energy trace when $\bar{\beta} > 1.2$ nm (Supplemental Figure S3), as all of these near-native, folded structures are similar in terms of solvation and protein-protein interactions.

In terms of the association process, the β path corresponds to the conformational selection model of coupled folding and binding. Following the red trace in Figure 8C from monomer to dimer, the monomers first adopt structures like those in the dimer, with attached B-chain C-terminal segments; they then approach one another, forming a variety of nonnative interfacial contacts that eventually collapse to the dimer-like set of native contacts. We note that the β path is consistent with the unbiased association trajectories simulated by Shaw and coworkers, who found that insulin dimer association is characterized by monomers, largely folded into their conformations in the dimer, forming near-native interfaces that eventually collapse to the native dimer interface.[33] Additionally, to remind the reader, the free energy profile, interfacial rotations, and monomeric unfolding observed along the α path are all consistent with the free energy minimum path discussed by Bagchi and coworkers.[30]

As mentioned previously, the α and β paths are limiting mechanisms from a broader ensemble of pathways (Supplemental Figure S1), a few of which are shown schematically in Figure 9. A variety of intermediate pathways are thus possible, and our data suggest that these pathways combine the behaviors observed along the limiting paths. For example, the green path in Figure 9 initially exhibits a partial separation and solvation of the β interface, but then otherwise exhibits behaviors similar to the those found along the α path. Specifically, the α helices twist away from one another, the B chain C-terminal strands detach from the nearby α helices and only then fully separate. All this occurs with a partially solvated β interface. As mentioned in a previous section, both partially solvated and partially unfolded species along this path are consistent with previous experimental studies.[25,29] In contrast, the pink path in Figure 9 initially follows the α path, then switches to exhibit behaviors more characteristic of the β path. The α helices partially twist away from one another, and then the B chain C-terminal strands separate while still attached to the α helices. This intermediate path is itself consistent with the biased association trajectories from Shaw and coworkers.[33] These trajectories primarily exhibit interfacial rotations and nonnative interactions (namely, Ser^{B9}:$Ser^{B'9}$) similar to the α path, but notably lack any substantial B-chain C-terminal detachment. Thus, the collective variables we identified enabled us to obtain an ensemble of paths that encompass the diversity seen in previous studies.[25,29,30,33]

Simulations enable determination of optimal isotopic labeling sites for infrared spectroscopy.

Even though the α and β paths are only limiting cases, most of the paths in Supplemental Figure S1 initially follow one of these limiting paths. As discussed previously, the initial steps along the α and β paths correspond to solvation of the α and β interfaces, respectively. In particular, the α path consists first of the solvation of the α interface, followed by the solvation of the β interface; the β path reverses this ordering. Thus, these simulation results can be further investigated by experimental techniques that can resolve residue-level solvation.

Fourier-transform (FT) and two-dimensional (2D) amide-I infrared (IR) spectroscopies are useful for studying protein secondary structure and solvation because they are sensitive probes of the hydrogen bonding of the carbonyl groups in protein backbones. In particular, one typical hydrogen bond to an amide carbonyl causes a redshift of about 16 cm^{-1}.[66] This means the location of the carbonyl stretch is sensitive to the number and strength of hydrogen bonds made by the backbone carbonyls, which includes hydrogen bonds associated with both secondary structure and protein-solvent interactions. Moreover, one can isotopically label specific amide carbonyl groups with $^{13}C^{18}O$, redshifting their vibrations by 65 cm^{-1} to isolate them from the other amide vibrations. Both 2D and 1D IR spectra can be generated through molecular modeling, effectively "mapping" the classical variables from molecular trajectories into a quantum-mechanical Hamiltonian (see ref. 66 for further review of 2DIR methods and their simulation).

These simulated spectra have been used to interpret both equilibrium and T-jump measurements of protein folding.[83] Furthermore, recent spectral simulation work from Meuwly and coworkers has shown that isotope labeled spectra for both the insulin dimer and monomer are qualitatively sensitive to the number of waters hydrating the labeled backbone carbonyl group.[84] They note, however, that no one structural feature is particularly strongly correlated to spectroscopic behavior, which is instead sensitive to the rapidly fluctuating environment around each backbone oscillator. When considering how best to experimentally probe the dynamics of the dissociation, it is thus difficult to *a priori* suggest the best sites to label. In previous sections, we discussed our results in the context of previous equilibrium[24] and T-jump[25] experiments of unlabeled insulin. Below, we combine our umbrella sampling results with additional simulations of IR spectra to propose new sites for isotopic labeling, with a view toward achieving residue-specific characterization of the dimer dissociation mechanism.

We expected the most promising sites for isotopic labeling to be at the dimer interface, as the participating residues exhibit large changes in SASA upon dissociation (Figure 7). Owing to the computational cost of 2DIR simulations, we first simulated FTIR spectra along both limiting paths for all possible constructs with a single interfacial residue isotopically labeled (between Ser^{B9} and Ala^{B30}). This process, summarized in the Supplemental Information (see Supplemental Figure S2), revealed that the isotopic labels that produce simulated spectra most sensitive to solvation are those on the residues in the previously identified hydrophobic core. For clarity, we focus on two specific residues: Phe^{B24}, at the β interface, and Glu^{B13}, at the α interface. A construct with the former label was studied in refs. 84 and 68, while, to the best of our knowledge, a construct with the latter label was not previously synthesized. For each label, we identify and simulate 2DIR for three states: the dimeric state, the monomeric state, and the solvated state (Figure 10). The solvated states for the Phe^{B24} and Glu^{B13} labels represent partially dissociated species with solvated β and α interfaces, respectively. The process of defining these solvated states is described in the Supplemental Information (Supplemental Figure S2).

For insulin labeled at Phe^{B24} (at the β interface, shown in Figure 10A), there is a strong peak at 1595 cm^{-1} in the dimer spectrum. This feature decreases in intensity, becomes redshifted to 1582 cm^{-1}, and broadens significantly along the diagonal as the carbonyl group of Phe^{B24}

becomes solvated (Figure 10B), consistent with previous measurements on the monomer.[68] Microscopically, we interpret the changes to reflect the hydrogen bond between Phe^{B24} and $Tyr^{B'26}$ breaking and the backbone becoming solvated. This behavior was observed once $\bar{\beta} \gtrsim 0.9$ nm along both the α and β paths (Supplemental Figure S2), suggesting that 2DIR experiments using this label should serve as a probe for the solvation of the β interface regardless of the dissociation mechanism. For most regions of the collective variable space, the redshifting and broadening of the peak occur together, but along the β path at $\bar{\beta} \in [0.75, 0.9]$ nm, the redshifting precedes the broadening. This corresponds to the interfacial hydrogen bonds breaking prior to solvation of the Phe^{B24} backbone carbonyl (Figure 7). Similarly, for insulin labeled at Glu^{B13} (at the α interface, shown in Figure 10C), we see a peak at 1595 cm^{-1}, and it becomes redshifted to 1579 cm^{-1} and broadens along the diagonal as the site containing the label becomes solvated (Figure 10D). Again, this behavior was observed along both the α and the β paths (Supplemental Figure S2).

By using temperature-jump IR spectroscopy and singular value decomposition as in ref. 25, one can decompose the time series of IR spectra into time-dependent weights of specific spectral components that correlate with molecular features. Our results show that the primary protein component for isotope-labeled spectra would correspond to interfacial solvation of the labeled residue. By measuring the contribution of this component to the overall spectra as a function of time, one can determine the characteristic timescale(s) of solvation for the labeled residue. Thus, by using a construct with the Glu^{B13} isotopic label in a T-jump IR experiment, one should be able to determine a distribution of timescales for α interface solvation by monitoring the relative contribution of the corresponding spectral component. Similarly, one can separately use T-jump IR measurements on a construct with the Phe^{B24} isotope label to measure the distribution of timescales for β interface solvation. By comparing these two distributions, one could determine the order of events during dissociation and in turn if one limiting mechanism or the other predominates; broad, temporally-overlapping distributions for α helix and β sheet interfacial solvations would be consistent with the diverse ensemble of energetically similar paths we see here. However, slight differences in these distributions could provide insights into preferred pathways, or one particular mechanism could dominate due to kinetic effects not explicitly considered by our simulations.

Conclusions

A key step in insulin function is its dissociation from dimer to monomer form, and an understanding of this process can aid in design of molecular analogs with desired properties. The practical importance of understanding insulin dimer dissociation has in turn made this system a paradigm for study of complex molecular recognition reactions. Here, we assembled a computational pipeline of methods for the study of complex molecular dynamics and applied it to understanding how the insulin dimer dissociates. This pipeline enabled us to identify collective variables that could promote dissociation with a minimum of monomeric unfolding. The resulting simulations revealed a previously unappreciated diversity of dissociation pathways with comparable free energy barriers. The limiting pathways, in which either the interfacial α helices separate and are solvated first (the α path) or the interfacial β strands separate and are solvated first (the β path), correspond to induced

fit and conformational selection mechanisms when considering them from the perspective of association. The similarities in barrier heights for qualitatively different pathways makes clear the importance of achieving chemical precision in the simulations, and an error estimator that we recently introduced allowed us to do so efficiently.

Along the two limiting pathways, the elements at the dimer interface rotate relative to each other as the monomers come apart. Along the energetically preferred α path, the rotation allows the formation of nonnative interactions involving residues on the interfacial α helices; this enables the C-terminal segment of insulin B chain to detach from the nearby interfacial α helix, thereby coupling monomeric unfolding to unbinding. No such unfolding is observed along the β path. The diversity of paths that we observe encompasses paths previously observed in simulation studies;[30,33] in this sense, our work reconciles seemingly discordant results in the literature.

Molecular simulations can guide the design and interpretation of experiments. The pathways that we observe provide a microscopic picture of a partially unfolded intermediate with conserved secondary structure previously suggested by T-jump experiments, though differences in conditions between the simulations and experiments make this picture tentative. With a view towards obtaining additional experimental constraints on the mechanism, we use the simulations to test possible sites for isotopic labeling for IR spectroscopy experiments. We predict that two sites in particular, Phe^{B24} and Glu^{B13}, should enable sensitive characterization of the solvation of the interfacial α helices and β strands. Our results thus provide insight into how to pursue the next generation of experiments to achieve residue-level resolution of the dissociation mechanism.

Supplementary Material

Refer to Web version on PubMed Central for supplementary material.

Acknowledgments

The authors thank John Strahan, Chatipat Lorpaiboon, Biman Bagchi, and Michael Weiss for helpful discussions. We thank Albert Pan, Bryan Jackson, and coworkers at D.E. Shaw for providing their trajectories for comparison. This work was supported by National Institutes of Health awards R01GM109455-01 and 5R01GM118774-02. Computations were performed on resources provided by the University of Chicago Research Computing Center, and the Extreme Science and Engineering Discovery Environment[85] (NSF Grant ACI-1548562) Bridges (PSC) computing nodes through allocation TG-MCB180007.

References

(1). Surprenant A; North RA Signaling at Purinergic P2X Receptors. Annu. Rev. Physiol 2009, 71, 333–359. [PubMed: 18851707]

(2). Baxter RC How IGF-1 Activates its Receptor. J. Cell Commun. Signaling 2015, 9, 87.

(3). De Meyts P Insulin/Receptor Binding: The Last Piece of the Puzzle? What Recent Progress on the Structure of the Insulin/Receptor Complex Tells Us (Or Not) About Negative Cooperativity and Activation. BioEssays 2015, 37, 389–397. [PubMed: 25630923]

(4). Dafforn TR; Smith CJI Natively Unfolded Domains in Endocytosis: Hooks, Lines and Linkers. EMBO Rep. 2004, 5, 1046–1052. [PubMed: 15520805]

(5). Koshland DE The Key–Lock Theory and the Induced Fit Theory. Angew. Chem., Int. Ed. Engl 1995, 33, 2375–2378.

(6). Levy Y; Cho SS; Onuchic JN; Wolynes PG A Survey of Flexible Protein Binding Mechanisms and their Transition States Using Native Topology Based Energy Landscapes. J. Mol. Biol 2005, 346, 1121–1145. [PubMed: 15701522]

(7). Schreiber G; Haran G; Zhou H-X Fundamental Aspects of Protein-Protein Association Kinetics. Chem. Rev 2009, 109, 839–860. [PubMed: 19196002]

(8). Csermely P; Palotai R; Nussinov R Induced Fit, Conformational Selection and Independent Dynamic Segments: an Extended View of Binding Events. Trends Biochem. Sci 2010, 35, 539–546. [PubMed: 20541943]

(9). Plattner N; Doerr S; De Fabritiis G; Noé F Complete protein-protein association kinetics in atomic detail revealed by molecular dynamics simulations and Markov modelling. Nat. Chem 2017, 9, 1005–1011. [PubMed: 28937668]

(10). Paul F; Noe F; Weikl TR Identifying Conformational-Selection and Induced-Fit Aspects in the Binding-Induced Folding of PMI from Markov State Modeling of Atomistic Simulations. J. Phys. Chem. B 2018, 122, 5649–5656. [PubMed: 29522679]

(11). Vashisth H; Abrams CF Docking of Insulin to a Structurally Equilibrated Insulin Receptor Ectodomain. Proteins: Struct., Funct., Bioinf 2010, 78, 1531–1543.

(12). Vashisth H; Abrams CF All-atom Structural Models of Insulin Binding to the Insulin Receptor in the Presence of a Tandem Hormone-Binding Element. Proteins: Struct., Funct., Bioinf 2013, 81, 1017–1030.

(13). Weiss MA; Lawrence MC A Thing of Beauty: Structure and Function of Insulin's "Aromatic Triplet". Diabetes, Obes. Metab 2018, 20, 51–63. [PubMed: 30230175]

(14). Ivanova MI; Sievers SA; Sawaya MR; Wall JS; Eisenberg D Molecular Basis for Insulin Fibril Assembly. Proc. Natl. Acad. Sci 2009, 106, 18990–18995. [PubMed: 19864624]

(15). Chen H; Shi M; Guo ZY; Tang YH; Qiao ZS; Liang ZH; Feng YM Four New Monomeric Insulins Obtained by Alanine Scanning the Dimer-Forming Surface of the Insulin Molecule. Protein Eng. 2000, 13, 779–782. [PubMed: 11161109]

(16). Zoete V; Meuwly M; Karplus M Study of the Insulin Dimerization: Binding Free Energy Calculations and per-Residue Free Energy Decomposition. Proteins: Struct., Funct., Bioinf 2005, 61, 79–93.

(17). Gong Q; Zhang H; Zhang H; Chen C Calculating the Absolute Binding Free Energy of the Insulin Dimer in an Explicit Solvent. RSC Adv. 2020, 10, 790–800.

(18). DeFelippis MR; Chance RE; Frank BH Insulin Self-Association and the Relationship to Pharmacokinetics and Pharmacodynamics. Crit. Rev. Ther. Drug Carrier Syst 2001, 18, 201–64. [PubMed: 11325032]

(19). Zoete V; Meuwly M; Karplus M A Comparison of the Dynamic Behavior of Monomeric and Dimeric Insulin Shows Structural Rearrangements in the Active Monomer. J. Mol. Biol 2004, 342, 913–929. [PubMed: 15342246]

(20). Jørgensen AMM; Kristensen SM; Led JJ; Balschmidt P Three-Dimensional Solution Structure of an Insulin Dimer: A Study of the B9(Asp) Mutant of Human Insulin using Nuclear Magnetic Resonance, Distance Geometry and Restrained Molecular Dynamics. J. Mol. Biol 1992, 227, 1146–1163. [PubMed: 1433291]

(21). Keller D; Clausen R; Josefsen K; Led JJ Flexibility and Bioactivity of Insulin: an NMR Investigation of the Solution Structure and Folding of an Unusually Flexible Human Insulin Mutant with Increased Biological Activity. Biochemistry 2001, 40, 10732–10740. [PubMed: 11524020]

(22). Bocian W; Sitkowski J; Bednarek E; Tarnowska A; Kawęcki R; Kozerski L Structure of Human Insulin Monomer in Water/Acetonitrile Solution. J. Biomol. NMR 2008, 40, 55–64. [PubMed: 18040865]

(23). Legge F; Budi A; Treutlein H; Yarovsky I Protein Flexibility: Multiple Molecular Dynamics Simulations of Insulin Chain B. Biophys. Chem 2006, 119, 146–157. [PubMed: 16129550]

(24). Ganim Z; Jones KC; Tokmakoff A Insulin Dimer Dissociation and Unfolding Revealed by Amide I Two-Dimensional Infrared Spectroscopy. Phys. Chem. Chem. Phys 2010, 12, 3579–3588. [PubMed: 20336256]

(25). Zhang XX; Jones KC; Fitzpatrick A; Peng CS; Feng CJ; Baiz CR; Tokmakoff A Studying Protein-Protein Binding through T-Jump Induced Dissociation: Transient 2D IR Spectroscopy of Insulin Dimer. J. Phys. Chem. B 2016, 120, 5134–5145. [PubMed: 27203447]

(26). Singh R; Bansal R; Rathore AS; Goel G Equilibrium Ensembles for Insulin Folding from Bias-Exchange Metadynamics. Biophys. J 2017, 112, 1571–1585. [PubMed: 28445749]

(27). Menting JG; Whittaker J; Margetts MB; Whittaker LJ; Kong GK; Smith BJ; Watson CJ; Žáková L; Kletvíková E; Jiráček J et al. How Insulin Engages its Primary Binding Site on the Insulin Receptor. Nature 2013, 493, 241–245. [PubMed: 23302862]

(28). Menting JG; Yang Y; Chan SJ; Phillips NB; Smith BJ; Whittaker J; Wickramasinghe NP; Whittaker LJ; Pandyarajan V; Wan Z. l. et al. Protective Hinge in Insulin Opens to Enable its Receptor Engagement. Proc. Natl. Acad. Sci 2014, 111, E3395–E3404. [PubMed: 25092300]

(29). Rimmerman D; Leshchev D; Hsu DJ; Hong J; Kosheleva I; Chen LX Direct Observation of Insulin Association Dynamics with Time-Resolved X-ray Scattering. J. Phys. Chem. Lett 2017, 8, 4413–4418. [PubMed: 28853898]

(30). Banerjee P; Mondal S; Bagchi B Insulin Dimer Dissociation in Aqueous Solution: A Computational Study of Free Energy Landscape and Evolving Microscopic Structure Along the Reaction Pathway. J. Chem. Phys 2018, 149, 114902. [PubMed: 30243274]

(31). Banerjee P; Mondal S; Bagchi B Effect of Ethanol on Insulin Dimer Dissociation. J. Chem. Phys 2019, 150, 084902. [PubMed: 30823756]

(32). Banerjee P; Bagchi B Dynamical Control by Water at a Molecular Level in Protein Dimer Association and Dissociation. Proc. Natl. Acad. Sci 2020, 117, 2302–2308.

(33). Pan AC; Jacobson D; Yatsenko K; Sritharan D; Weinreich TM; Shaw DE Atomic-Level Characterization of Protein–Protein Association. Proc. Natl. Acad. Sci 2019, 116, 4244–4249. [PubMed: 30760596]

(34). Thiede EH; Van Koten B; Weare J; Dinner AR Eigenvector Method for Umbrella Sampling Enables Error Analysis. J. Chem. Phys 2016, 145, 084115. [PubMed: 27586912]

(35). Dinner AR; Thiede E; Van Koten B; Weare J Stratification as a General Variance Reduction Method for Markov Chain Monte Carlo. arXiv Preprint 2017, arXiv:1705.08445.

(36). MacKerell AD; Bashford D; Bellott M; Dunbrack RL; Evanseck JD; Field MJ; Fischer S; Gao J; Guo H; Ha S et al. All-Atom Empirical Potential for Molecular Modeling and Dynamics Studies of Proteins. J. Phys. Chem. B 1998, 102, 3586–3616. [PubMed: 24889800]

(37). Best RB; Zhu X; Shim J; Lopes PEM; Mittal J; Feig M; MacKerell AD Optimization of the Additive CHARMM All-Atom Protein Force Field Targeting Improved Sampling of the Backbone ϕ, ψ and Side-Chain χ_1 and χ_2 Dihedral Angles. J. Chem. Theory Comput 2012, 8, 3257–3273. [PubMed: 23341755]

(38). Huang J; Rauscher S; Nawrocki G; Ran T; Feig M; De Groot BL; Grubmüller H; MacKerell AD CHARMM36m: An Improved Force Field for Folded and Intrinsically Disordered Proteins. Nat. Methods 2016, 14, 71–73. [PubMed: 27819658]

(39). Abraham MJ; Murtola T; Schulz R; Páll S; Smith JC; Hess B; Lindah E GROMACS: High Performance Molecular Simulations Through Multi-Level Parallelism from Laptops to Supercomputers. SoftwareX 2015, 1–2, 19–25.

(40). Jo S; Kim T; Iyer VG; Im W CHARMM-GUI: A Web-Based Graphical User Interface for CHARMM. J. Comput. Chem 2008, 29, 1859–1865. [PubMed: 18351591]

(41). Lee J; Cheng X; Swails JM; Yeom MS; Eastman PK; Lemkul JA; Wei S; Buckner J; Jeong JC; Qi Y et al. CHARMM-GUI Input Generator for NAMD, GROMACS, AMBER, OpenMM, and CHARMM/OpenMM Simulations Using the CHARMM36 Additive Force Field. J. Chem. Theory Comput 2016, 12, 405–413. [PubMed: 26631602]

(42). Goga N; Rzepiela AJ; De Vries AH; Marrink SJ; Berendsen HJ Efficient Algorithms for Langevin and DPD Dynamics. J. Chem. Theory Comput 2012, 8, 3637–3649. [PubMed: 26593009]

(43). Hess B; Bekker H; Berendsen HJ; Fraaije JG LINCS: A Linear Constraint Solver for Molecular Simulations. J. Comput. Chem 1997, 18, 1463–1472.

(44). Darden T; York D; Pedersen L Particle Mesh Ewald: An N·log(N) Method for Ewald Sums in Large Systems. J. Chem. Phys 1993, 98, 10089–10092.

(45). Humphrey W; Dalke A; Schulten K VMD: Visual Molecular Dynamics. J. Mol. Graphics 1996, 7855, 33–38.

(46). Phillips JC; Braun R; Wang W; Gumbart J; Tajkhorshid E; Villa E; Chipot C; Skeel RD; Kalé L; Schulten K Scalable Molecular Dynamics with NAMD. J. Comput. Chem 2005, 26, 1781–1802. [PubMed: 16222654]

(47). Sakabe N; Sakabe K; Sasaki K; Murayoshi M 0.92A structure of 2Zn human insulin at 100K. www.rcsb.org/structure/3w7y, 2013.

(48). Jorgensen WL; Chandrasekhar J; Madura JD; Impey RW; Klein ML Comparison of Simple Potential Functions for Simulating Liquid Water. J. Chem. Phys 1983, 79, 926–935.

(49). Beglov D; Roux B Finite Representation of an Infinite Bulk System: Solvent Boundary Potential for Computer Simulations. J. Chem. Phys 1994, 100, 9050–9063.

(50). Parrinello M; Rahman A Polymorphic Transitions in Single Crystals: A New Molecular Dynamics Method. J. Appl. Phys 1981, 52, 7182–7190.

(51). Isralewitz B; Gao M; Schulten K Steered Molecular Dynamics and Mechanical Functions of Proteins. Curr. Opin. Struct. Biol 2001, 11, 224–230. [PubMed: 11297932]

(52). Maragliano L; Fischer A; Vanden-Eijnden E; Ciccotti G String Method in Collective Variables: Minimum Free Energy Paths and Isocommittor Surfaces. J. Chem. Phys 2006, 125, 024106.

(53). Vanden-Eijnden E; Venturoli M Revisiting the Finite Temperature String Method for the Calculation of Reaction Tubes and Free Energies. J. Chem. Phys 2009, 130, 194103. [PubMed: 19466817]

(54). Weiss M Design of Ultra-Stable Insulin Analogues for the Developing World. J. Health Spec 2013, 1, 59–70.

(55). Van Koten B; Luskin M Stability and Convergence of the String Method for Computing Minimum Energy Paths. Multiscale Model. Simul 2019, 17, 873–898.

(56). Coifman RR; Lafon S Diffusion Maps. Appl. Comput. Harmonic Anal 2006, 21, 5–30.

(57). Berry T; Harlim J Variable Bandwidth Diffusion Kernels. Appl. Comput. Harmonic Anal 2016, 40, 68–96.

(58). Marchi M; Ballone P Adiabatic Bias Molecular Dynamics: A Method to Navigate the Conformational Space of Complex Molecular Systems. J. Chem. Phys 1999, 110, 3697–3702.

(59). Bonomi M; Branduardi D; Bussi G; Camilloni C; Provasi D; Raiteri P; Donadio D; Marinelli F; Pietrucci F; Broglia RA et al. PLUMED: A Portable Plugin for Free-Energy Calculations with Molecular Dynamics. Comput. Phys. Commun 2009, 180, 1961–1972.

(60). Tribello GA; Bonomi M; Branduardi D; Camilloni C; Bussi G PLUMED 2: New Feathers for an Old Bird. Comput. Phys. Commun 2014, 185, 604–613.

(61). Bonomi M; Bussi G; Camilloni C; Tribello GA; Banáš P; Barducci A; Bernetti M; Bolhuis PG; Bottaro S; Branduardi D et al. Promoting Transparency and Reproducibility in Enhanced Molecular Simulations. Nat. Methods 2019, 16, 670–673. [PubMed: 31363226]

(62). Park S; Kim T; Im W Transmembrane Helix Assembly by Window Exchange Umbrella Sampling. Phys. Rev. Lett 2012, 108, 108102. [PubMed: 22463457]

(63). Park S; Im W Two Dimensional Window Exchange Umbrella Sampling for Transmembrane Helix Assembly. J. Chem. Theory Comput 2013, 9, 13–17. [PubMed: 23486635]

(64). Sugita Y; Kitao A; Okamoto Y Multidimensional Replica-Exchange Method for Free-Energy Calculations. J. Chem. Phys 2000, 113, 6042–6051.

(65). Moradi M Codes and Scripts, Theoretical and Computational Biophysics Group. https://www.ks.uiuc.edu/mahmoud/codes.html. (accessed July 15, 2019).

(66). Reppert M; Tokmakoff A Computational Amide I 2D IR Spectroscopy as a Probe of Protein Structure and Dynamics. Annu. Rev. Phys. Chem 2016, 67, 359–386. [PubMed: 27023758]

(67). Feng CJ; Dhayalan B; Tokmakoff A Refinement of Peptide Conformational Ensembles by 2D IR Spectroscopy: Application to Ala–Ala–Ala. Biophys. J 2018, 114, 2820–2832. [PubMed: 29925019]

(68). Dhayalan B; Fitzpatrick A; Mandal K; Whittaker J; Weiss MA; Tokmakoff A; Kent SBH Efficient Total Chemical Synthesis of 13 C= 18 O Isotopomers of Human Insulin for Isotope-Edited FTIR. ChemBioChem 2016, 17, 415–420. [PubMed: 26715336]

(69). Reppert M; Tokmakoff A Communication: Quantitative Multi-Site Frequency Maps for Amide I Vibrational Spectroscopy. J. Chem. Phys 2015, 143, 061102. [PubMed: 26277120]

(70). la Cour Jansen T; Dijkstra AG; Watson TM; Hirst JD; Knoester J Modeling the Amide I Bands of Small Peptides. J. Chem. Phys 2006, 125, 44312. [PubMed: 16942147]

(71). la Cour Jansen T; Knoester J A Transferable Electrostatic Map for Solvation Effects on Amide I Vibrations and its Application to Linear and Two-Dimensional Spectroscopy. J. Chem. Phys 2006, 124, 044502. [PubMed: 16460180]

(72). Hamm P; Lim M; Hochstrasser RM Structure of the Amide I Band of Peptides Measured by Femtosecond Nonlinear-Infrared Spectroscopy. J. Phys. Chem. B 1998, 102, 6123–6138.

(73). Torii H Effects of Intermolecular Vibrational Coupling and Liquid Dynamics on the Polarized Raman and Two-Dimensional Infrared Spectral Profiles of Liquid N,N-Dimethylformamide Analyzed with a Time-Domain Computational Method. J. Phys. Chem. A 2006, 110, 4822–4832. [PubMed: 16599451]

(74). Liang C; Jansen TL An Efficient N(3)-Scaling Propagation Scheme for Simulating Two-Dimensional Infrared and Visible Spectra. J. Chem. Theory. Comput 2012, 8, 1706–1713. [PubMed: 26593664]

(75). Feng CJ; Tokmakoff A The Dynamics of Peptide-Water Interactions in Dialanine: An Ultrafast Amide I 2D IR and Computational Spectroscopy Study. J. Chem. Phys 2017, 147, 085101. [PubMed: 28863528]

(76). Raghunathan S; El Hage K; Desmond JL; Zhang L; Meuwly M The Role of Water in the Stability of Wild-type and Mutant Insulin Dimers. J. Phys. Chem. B 2018, 122, 7038–7048. [PubMed: 29916244]

(77). Crick F The Packing of α-Helices: Simple Coiled-Coils. Acta Crystallogr. 1953, 6, 689–697.

(78). Richmond TJ; Richards FM Packing of α-Helices: Geometrical Constraints and Contact Areas. J. Mol. Biol 1978, 119, 537–555. [PubMed: 642001]

(79). Chothia C; Levitt M; Richardson D Helix to Helix Packing in Proteins. J. Mol. Biol 1981, 145, 215–250. [PubMed: 7265198]

(80). Frishman D; Argos P Knowledge-Based Protein Secondary Structure Assignment. Proteins: Struct., Funct., Genet 1995, 23, 566–579. [PubMed: 8749853]

(81). Scapin G; Dandey VP; Zhang Z; Prosise W; Hruza A; Kelly T; Mayhood T; Strickland C; Potter CS; Carragher B Structure of the Insulin Receptor-Insulin Complex by Single-Particle Cryo-EM Analysis. Nature 2018, 556, 122–125. [PubMed: 29512653]

(82). Glidden MD; Yang Y; Smith NA; Phillips NB; Carr K; Wickramasinghe NP; Ismail-Beigi F; Lawrence MC; Smith BJ; Weiss MA Solution Structure of an Ultra-Stable Single-Chain Insulin Analog Connects Protein Dynamics to a Novel Mechanism of Receptor Binding. J. Biol. Chem 2018, 293, 69–88. [PubMed: 29114034]

(83). Baiz CR; Lin Y-S; Peng CS; Beauchamp KA; Voelz VA; Pande VS; Tokmakoff A A Molecular Interpretation of 2D IR Protein Folding Experiments with Markov State Models. Biophys. J 2014, 106, 1359–1370. [PubMed: 24655511]

(84). Desmond JL; Koner D; Meuwly M Probing the Differential Dynamics of the Monomeric and Dimeric Insulin from Amide-I IR Spectroscopy. J. Phys. Chem. B 2019, 123, 6588–6598. [PubMed: 31318551]

(85). Towns J; Cockerill T; Dahan M; Foster I; Gaither K; Grimshaw A; Hazlewood V; Lathrop S; Lifka D; Peterson GD et al. XSEDE: Accelerating Scientific Discovery. Comput. Sci. Eng 2014, 16, 62–74.

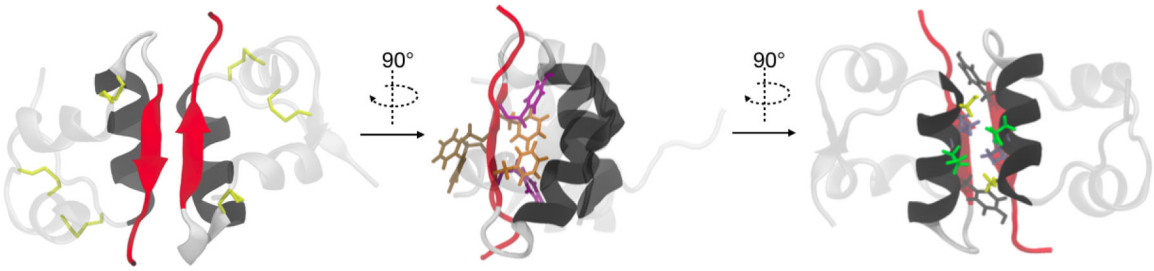

Figure 1:

Three views of the insulin dimer. The A chain and residues Phe^{B1}-Gly^{B8} of each monomer are shown in translucent silver, while interfacial residues are opaque. The interfacial α helices are shown in black, the β turn is shown in white, and the β sheet is shown in red. In the left panel, cysteine bonds are shown in yellow. In the middle panel, side chains for residues Phe^{B24} (orange), Phe^{B25} (brown), and Tyr^{B26} (purple) are shown. In the right panel, side chains for residues Ser^{B9} (yellow), Val^{B12} (blue), Glu^{B13} (green), and Tyr^{B16} (gray) are shown.

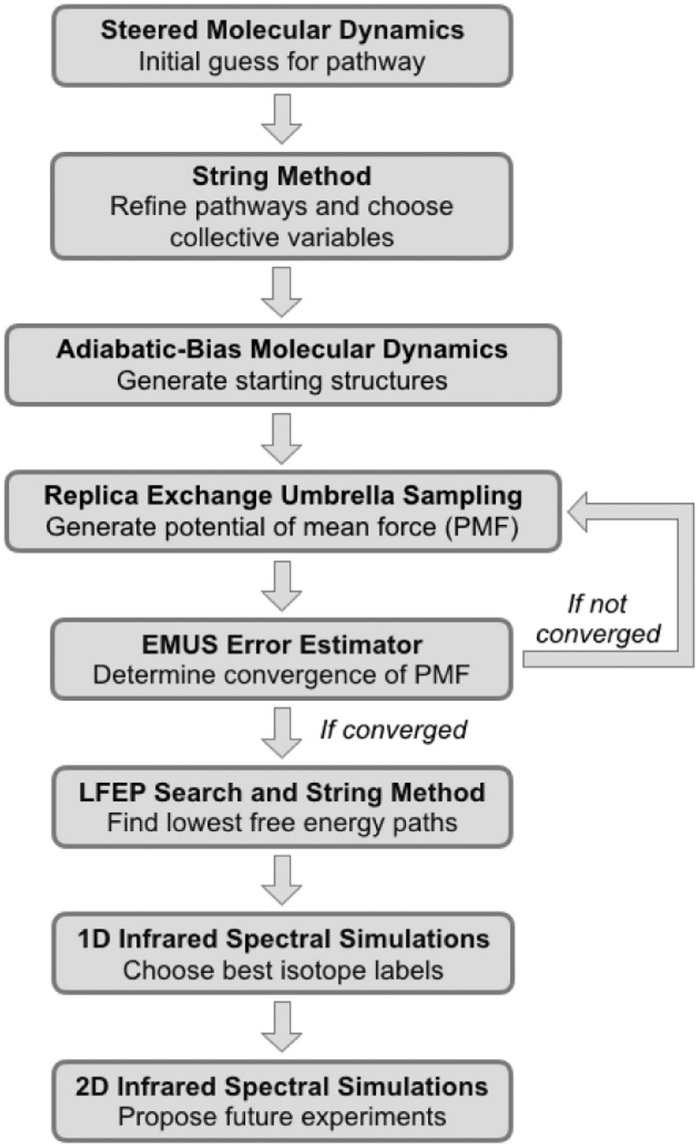

Figure 2:

An overview of the computational pipeline. Each panel shows the method used and the information it yields. See the Methods section for further details.

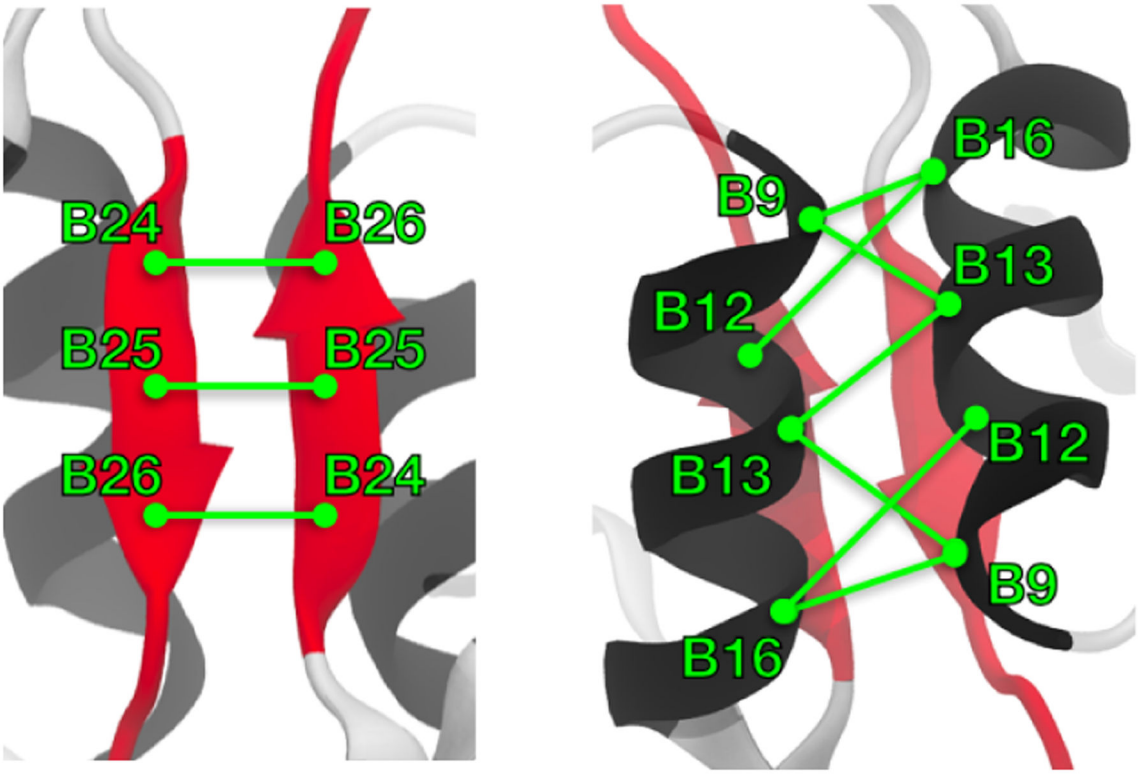

Figure 3:
Schematic showing the β sheet contact pairs (left) and the α helix contact pairs (right). These correspond to the similarly labeled rows of Supplemental Table S1.

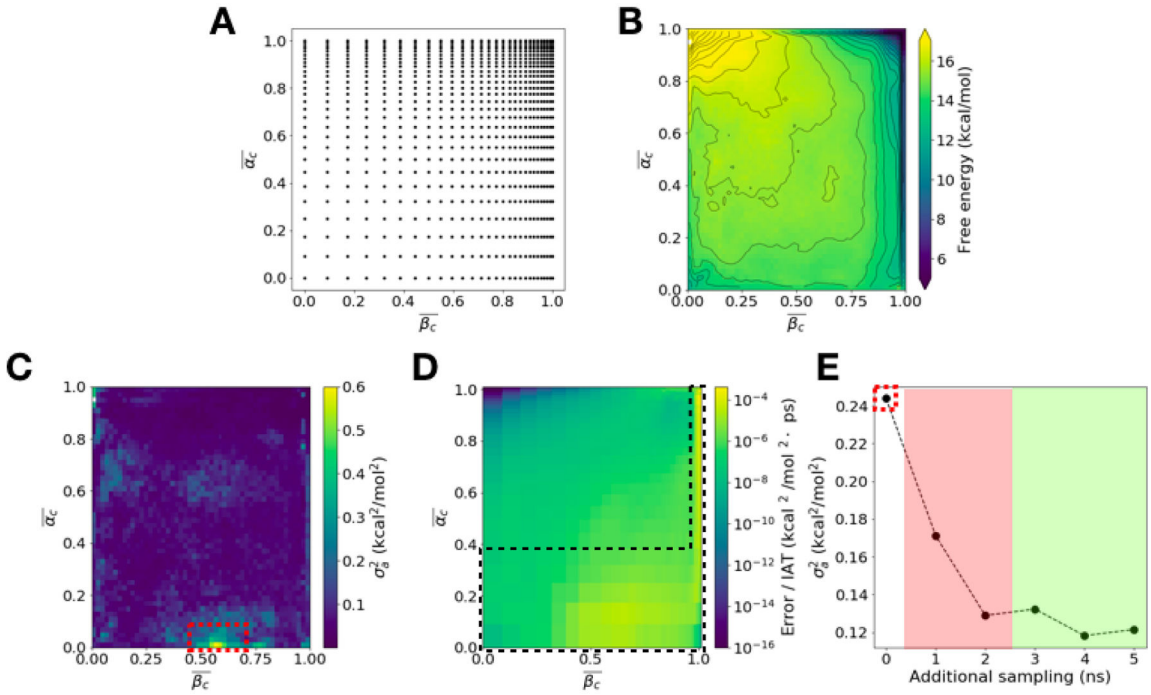

Figure 4:

Umbrella sampling. (A) The location of the window centers used for the REUS procedure, shown in the space of $\overline{\beta_c}$ and $\overline{\alpha_c}$. These are logarithmically spaced to place more density near the dimer (upper right corner). (B) Free energy as a function of the average numbers of β and α contacts at the insulin dimer interface (contour spacing 0.5 kcal/mol). 5 ns of sampling was gathered per window (784 windows). (C) The asymptotic variance associated with the free energy in (B). The region of highest variance, with average 0.25 and maximum 0.59 $kcal^2/mol^2$, is marked by the red box. (D) The per-window error contributions to the marked variance in (C), assuming that the matrix Σ is diagonal. 5 ns of additional sampling was added to only the boxed black area of large error contributions. (E) How the average asymptotic variance of the marked region in (C) decreased as 5 more ns of sampling was added per selected window. The red shaded region represents the area where the additional sampling is shorter than 10 times the autocorrelation time for EMUS quantities. The asymptotic variance data in this region is thus unreliable. Reliable asymptotic variances are obtained in the green shaded region.

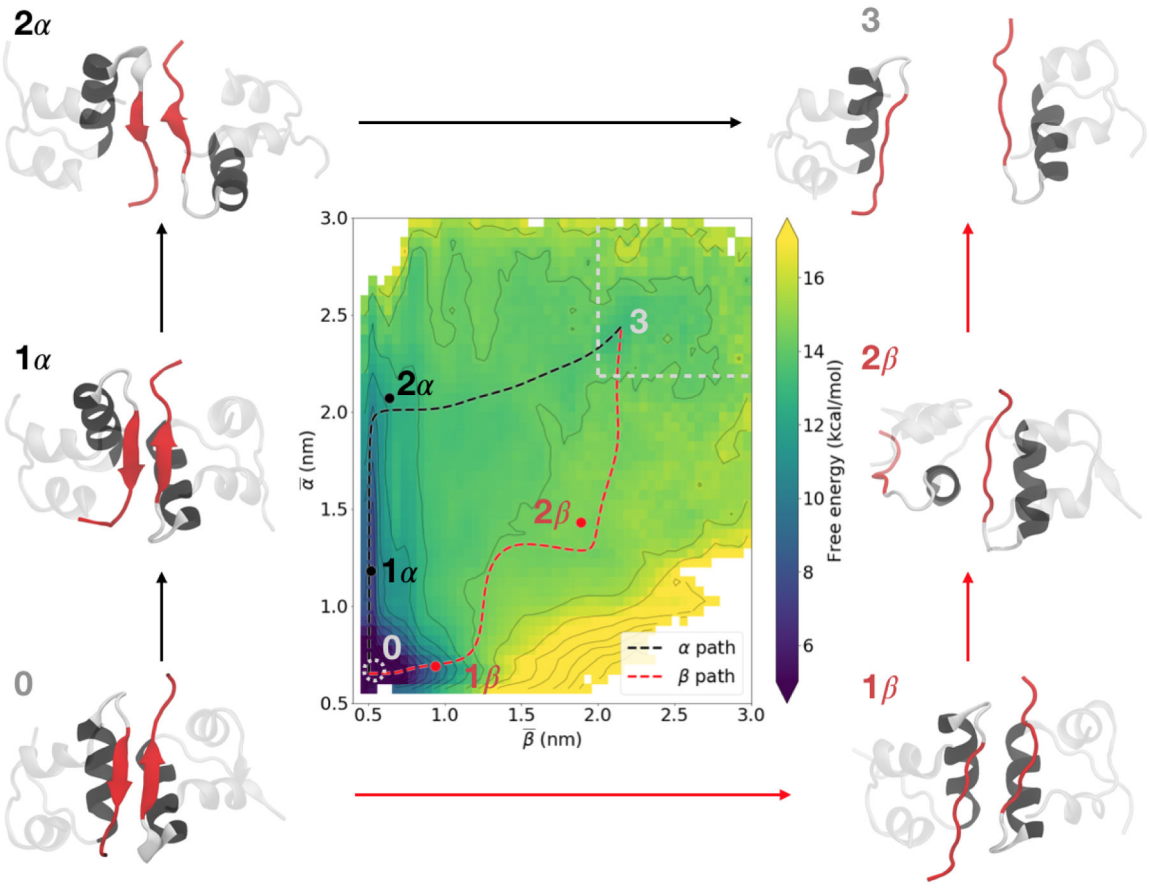

Figure 5:

Potential of mean force (PMF) as a function of $\bar{\alpha}$ and $\bar{\beta}$. Limiting mean free energy paths in which the interfacial α or β contacts break first are indicated by black and red dashed lines, respectively. Representative structures corresponding to the marked points along the paths are labeled and shown adjacent to the PMF. These structures are referenced throughout the paper and are available in the supplemental material. The dimer is marked by a dotted white circle, and the monomeric state is marked by a dotted white box. Contour lines are every 2 k_BT. The color scale is capped at both the upper and lower ends to more clearly show the variation in the partially-dissociated regime.

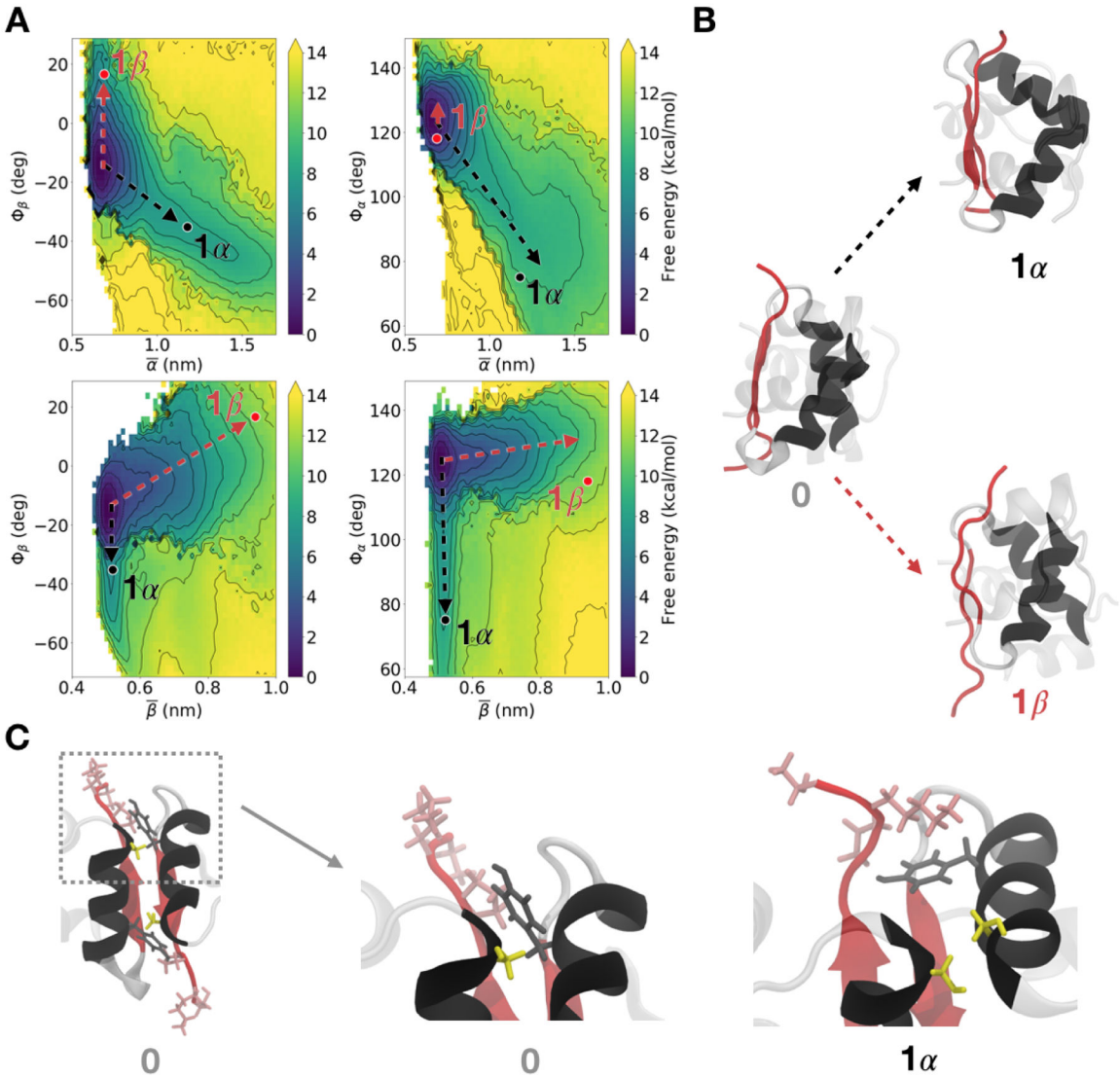

Figure 6:

The monomers rotate relative to each other during dissociation. (A) PMFs characterizing the rotations as pairwise functions of $\bar{\alpha}$ (top) or $\bar{\beta}$ (bottom), and Φ_β (left) or Φ_α (right). Superimposed arrows show the negative rotations associated with the α path (black) and the positive rotations associated with the β path (red). Intermediates are marked on the PMF, and are as labeled in Figure 5. Structures were chosen to show the rotation of Φ_β; for this reason, the arrows in the left plots terminate at the dots but those on the right plots do not. Contour lines are every 2 k_BT. The color scale was capped at 14 kcal/mol. (B) Representative structures for the rotations along the α and β paths, represented by the black and red arrows, respectively. These structures, labeled in (A), are the same as those labeled in Figure 5. (C) The dimer with the interfacial α helices in front, showing the side chains for Ser^{B9}, Tyr^{B16} (gray) and Pro^{B28}-Ala^{B30} (pink). Zooming in (middle), one can see the native contact of Ser^{B9}-$Tyr^{B'16}$, with Pro^{B28}-Ala^{B30} behind. Along the α path (right), $Tyr^{B'16}$ has rotated away from Ser^{B9}, and is instead in contact with Pro^{B28}-Ala^{B30}. Furthermore, this rotation brings Ser^{B9} and $Ser^{B'9}$ together.

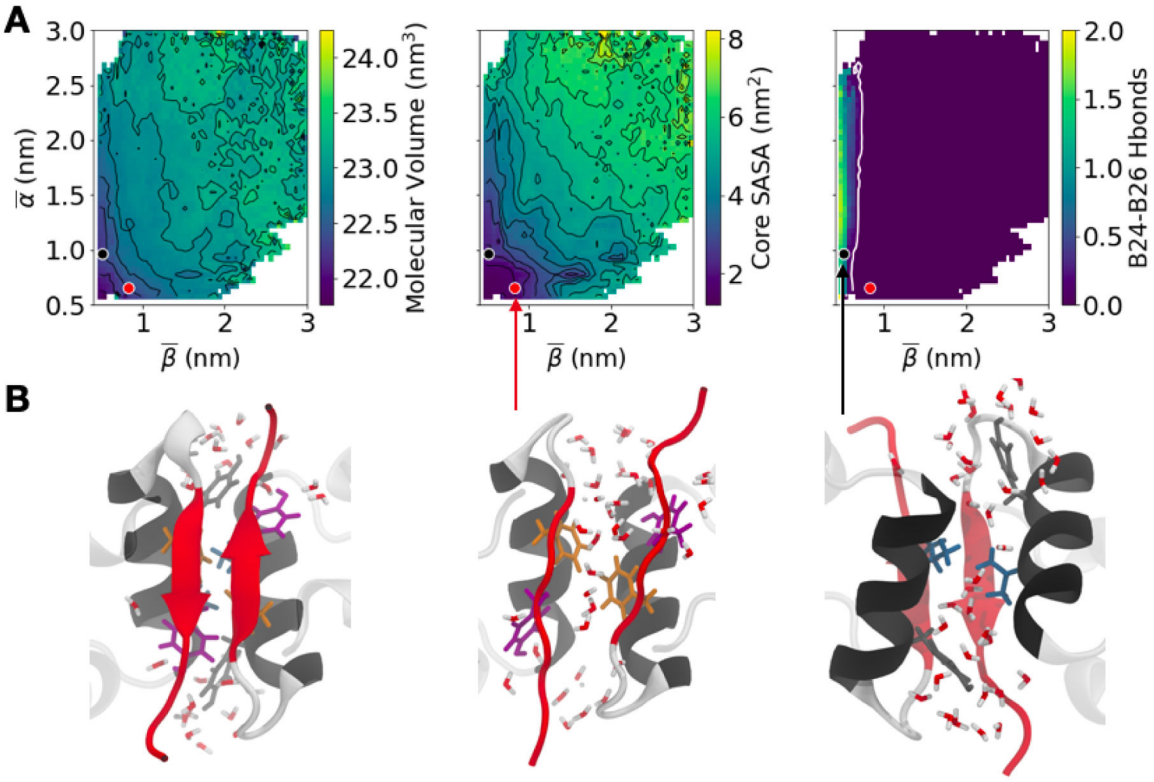

Figure 7:

Characterizing solvation. (A) Averages of total molecular volume (left), core SASA (middle), and number of interfacial Phe^{B24}-Tyr^{B26} hydrogen bonds (right) as a function of $\bar{\alpha}$ and $\bar{\beta}$. Contours are every 0.2 nm^3 and 0.5 nm^2 for the molecular volume and SASA plots, respectively. The white contour on the right plot indicates where the number of hydrogen bonds drops to 2% of the average in the dimer. (B) Insulin structures showing the unsolvated dimer interface (left), the solvation of the β interface (middle), and the solvation of the α interface (right). The locations of these structures are marked in (A).

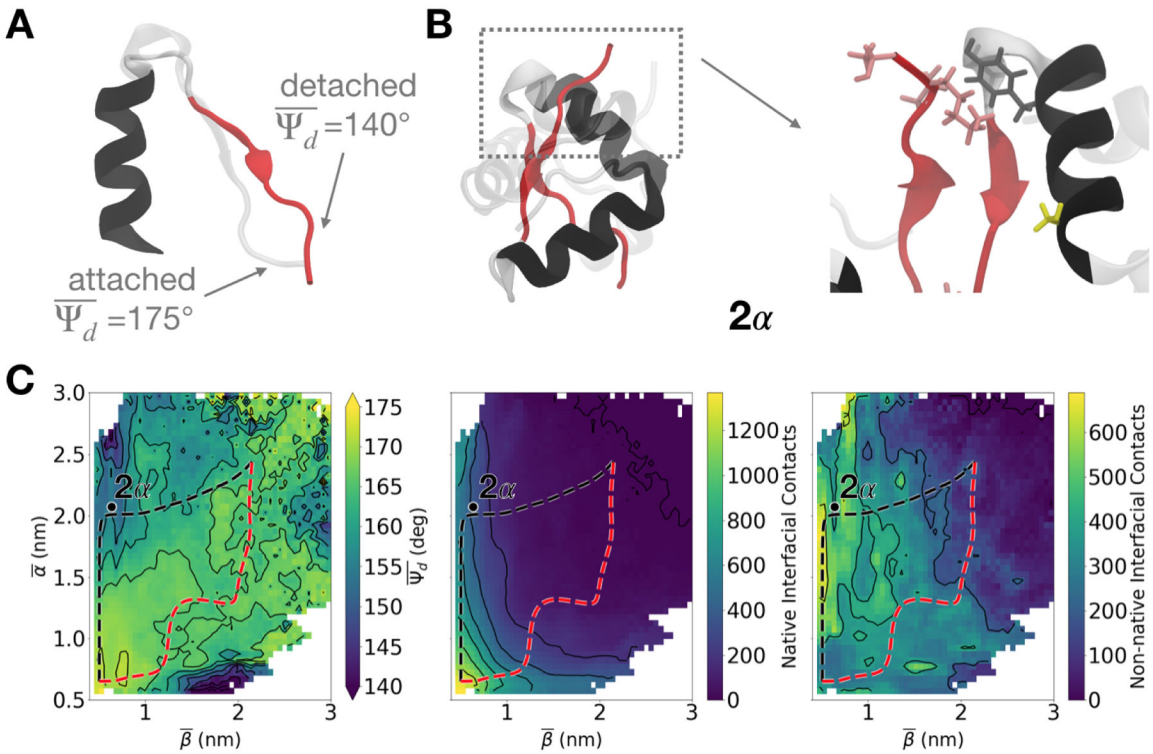

Figure 8:

Characterizing detachment. (A) A representative monomeric structure contrasting attached and detached B-chain C-terminal segments. (B) Structural depiction of how the detachment of the B-chain C-terminal segment allows for continued nonnative interactions between Pro^{B28}-Ala^{B30} and $Tyr^{B'16}$. (c) (Left) Average of $\overline{\Psi_d}$ as a function of $\bar{\alpha}$ and $\bar{\beta}$ with black contour lines shown every 5°. (Middle) Number of native non-hydrogen atom native interfacial contacts and (right) non-hydrogen atom nonnative interfacial contacts (cutoff 7 Å), with contour lines shown every 200 contacts. On all graphs, the α (black) and β (red) paths are shown, as is the location of structure 2α shown in (B).

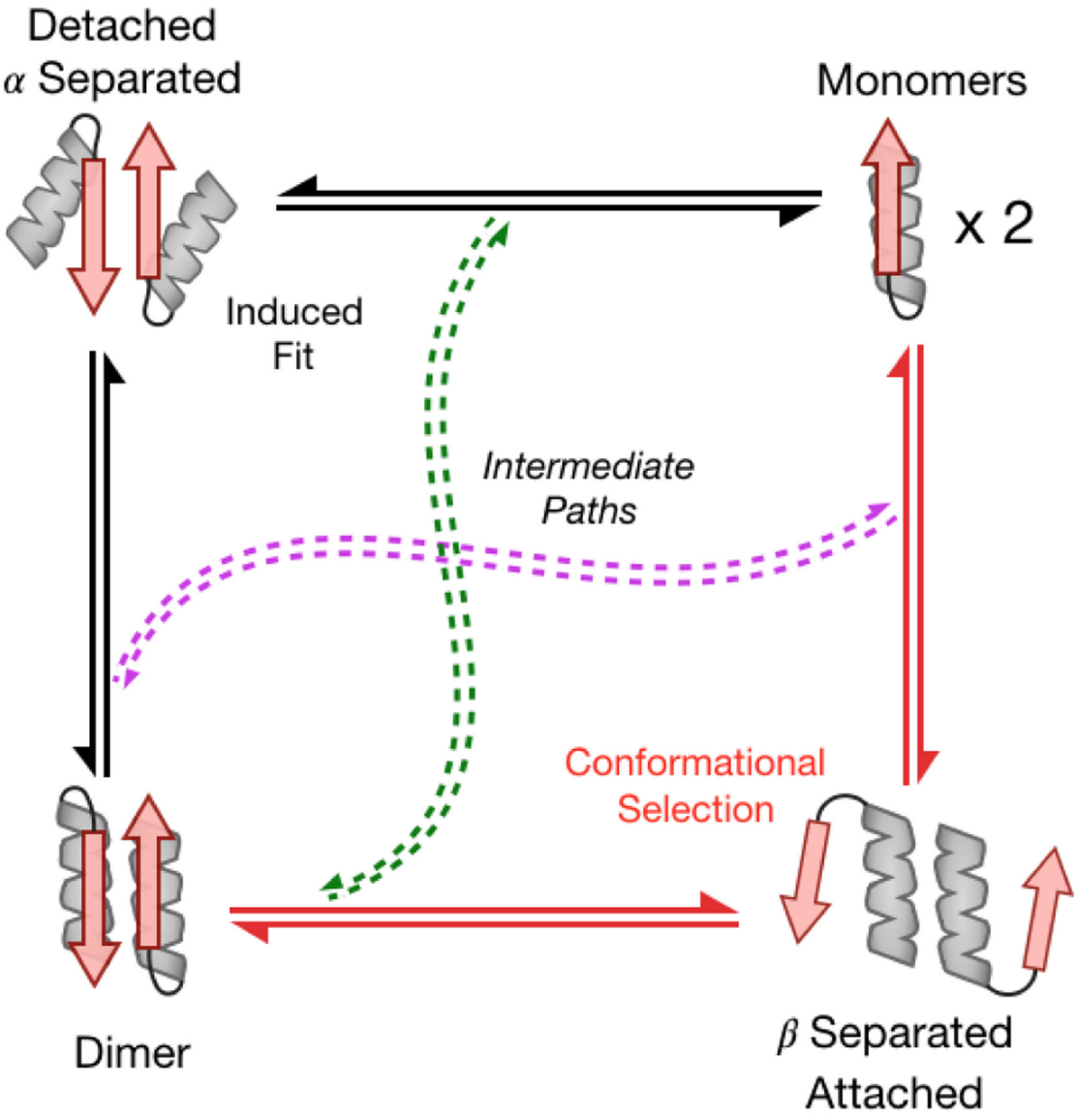

Figure 9:

A schematic representation of the pathways of insulin dimer dissociation/association, oriented as in Figure 5, and labeled to describe the limiting behaviors of coupled folding and binding. The α path is depicted by the black solid double arrows, and the β path is depicted by the red solid double arrows. Intermediate paths, shown by the dashed double arrows, are colored as in Supplemental Figure S1.

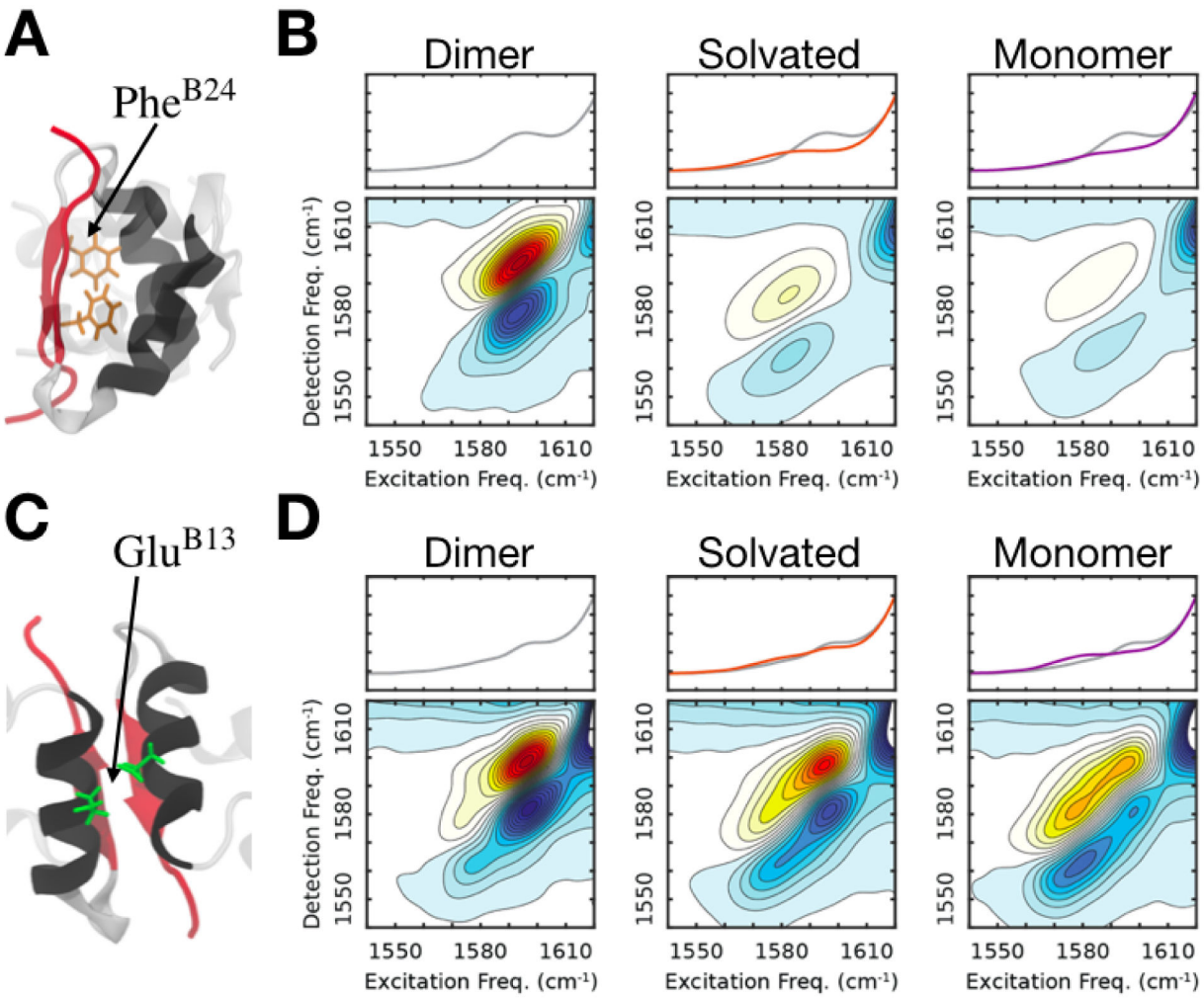

Figure 10:

Simulated IR spectra for selected isotopically labeled constructs. (A) Dimeric structure showing the Phe^{B24} side chain, which was isotopically labeled on its backbone carbonyl. (B) Simulated 2DIR spectra of the Phe^{B24}-labeled dimer (left), solvated species (middle), and monomer (right). Intensities are normalized using the peak intensity of the dimer spectrum, with the contours spaced by 7.5%. (C & D) Similar structures/spectra, but for the Glu^{B13} -labeled insulin. In both cases, the spectra for the solvated species were generated from structures along both the α and β paths.